Journal of Catalysis 258 (2008) 273–288

Contents lists available at ScienceDirect

Journal of Catalysis

www.elsevier.com/locate/jcat

Detailed kinetic modeling of NO_x storage and reduction with hydrogen as the reducing agent and in the presence of CO_2 and H_2O over a Pt/Ba/Al catalyst

Anna Lindholm [a], Neal W. Currier [b], Junhui Li [b], Aleksey Yezerets [b], Louise Olsson [a,*]

[a] Competence Centre for Catalysis, Chemical Reaction Engineering, Chalmers University of Technology, SE-412 96 Göteborg, Sweden
[b] Cummins Inc., 1900 McKinley Ave., MC 50183, Columbus, IN 47201, USA

ARTICLE INFO

Article history:
Received 26 February 2008
Revised 16 June 2008
Accepted 17 June 2008
Available online 17 July 2008

Keywords:
Detailed kinetic modeling
NO_x storage and reduction
Pt/Ba/Al
H_2
NH_3 formation
H_2O
CO_2

ABSTRACT

A detailed kinetic model of NO_x storage and reduction, in the presence of H_2O and CO_2, with hydrogen as the reducing agent was developed and validated in this study. The mechanism was derived from flow reactor experiments conducted at 200–400 °C over a Pt/Ba/Al monolith sample. The detailed kinetic model is divided into four sub-models: (i) NO oxidation over Pt, (ii) NO_x storage, (iii) NO_x reduction over Pt, and (iv) NO_x regeneration. The sub-model for NO_x storage is based on our earlier work and is further developed in this study to include high concentrations of CO_2 and H_2O in the feed and also low temperature storage. In the model NO_x is allowed to be stored on two different types of storage sites: $BaCO_3$ and a second storage site denoted S_3. Based on experimental results many studies suggests multiple storage sites one these catalysts, and there are different explanations (i) alumina and barium sites (ii) bulk and surface barium, (iii) barium close and far from the noble metal, etc. The disproportionation route, where NO_2 is stored over $BaCO_3$, is included in the NO_x storage model. To account for the storage occurring at lower temperatures NO can be stored over both $BaCO_3$ and S_3 in the presence of O_2. NO adsorbed over S_3 can be further oxidized to NO_2 by reacting with oxygen on neighboring Pt sites. The second storage site (S_3) is important in order to explain NO_x storage at low temperatures and the disproportionation reaction is essential to describe the storage at high temperatures. The NO_x reduction sub-model used here was developed earlier over Pt/Si. Additional to the reduction of NO_x into N_2, it describes the formation of NH_3 over Pt. In the sub-model describing the regeneration of NO_x, adsorbed NO_x species react with hydrogen adsorbed on Pt sites. Ammonia oxidation over Pt and reactions between surface species of barium and NH_3 according to ammonia selective catalytic reduction (SCR) chemistry are also incorporated in the regeneration sub-model. The full model can describe the complete uptake of NO_x in the beginning of the lean period, the NO_x breakthrough, and the slow NO_x storage in the end of the lean period very well as well as the following release and reduction. It can also predict the gradual decrease in the storage capacity occurring in lean/rich cycling experiments. Furthermore, the ammonia formation predicted by the model fits well with experimental data. The model was validated with short lean (60 s) and rich (15 s) cycles which were not included in the model development. The model could predict these experiments well for all three temperatures (200, 300 and 400 °C).

1. Introduction

The main advantages of diesel engines and lean-burn gasoline engines compared to conventional gasoline engines are the low fuel consumption and the reduced emissions of CO_2. However, due to the large excess of oxygen during the lean operation of these engines, the NO_x cannot be reduced over the conventional three-way catalyst. The NO_x storage and reduction technology (NSR) is a promising method to reduce nitrogen oxides in lean exhaust. This method was developed by Toyota in the 1990s [1]. The NSR catalyst works in a cyclic mode with alternating lean and rich periods. Nitrogen oxides are stored in the catalyst under the relatively long lean periods (minutes), during which the catalyst operates under oxygen excess. The catalyst is then regenerated for a short period of time (seconds) from the stored NO_x, by letting the engine operate in the rich mode (oxygen deficient) or by introducing a reducing agent upstream of the catalyst [2]. During the regeneration NO_x is released from the storage sites and reduced, with hydrocarbons (HC), H_2 and CO, to produce CO_2, H_2O and N_2. A typical NO_x storage and reduction catalyst consists of a high surface area support, a storage component and precious metals. A well studied catalyst formula for this application is Pt/Ba/Al.

* Corresponding author. Fax: +46 0 31 772 3035.
E-mail address: louise.olsson@chalmers.se (L. Olsson).

0021-9517/$ – see front matter
doi:10.1016/j.jcat.2008.06.022

In many studies in the literature it is suggested that oxidation of NO to NO_2 over the precious metal is the first step in NO_x storage [3–9] and that NO_2 is subsequently stored on the trapping material. However, Nova et al. [10–12] have described the mechanism of NO_x storage by two routes that operate simultaneously, the "nitrite route" and the "nitrate route." The nitrite route involves the direct uptake of NO in the presence of O_2 on the barium component, to form adsorbed nitrite species. The nitrites are then oxidized to nitrates. Simultaneously, NO oxidation to NO_2 can also occur, and the NO_2 formed can adsorb on barium in the form of nitrates via a disproportionation reaction (nitrate route).

Several publications have stressed that the proximity between Pt and Ba sites is very important for NO_x storage [1,10,12–15]; it has been suggested that the storage of NO_x is favored when Pt sites are close to Ba sites [10,15]. In addition, several investigations have indicated that NO_x can be stored over several types of storage sites [10,14,16].

When the reduction efficiency of different reducing agents, such as H_2, CO, C_3H_6 and C_3H_8, was investigated, it was concluded that H_2 is the most effective reductant [17–22]. In addition, H_2 is an active reducing agent at temperatures too low for other reductants to be active [21]. The products formed when using hydrogen as a reducing agent are NH_3, N_2O and N_2 [23,24]. According to Szailer et al. [22], the role of H_2 during the reduction is to keep the precious metal surface clean, for the dissociation of NO_x, by reacting with adsorbed oxygen to form H_2O. They also suggested that N_2 is formed by the recombination of adsorbed nitrogen atoms and that the formation of NH_3 occurs due to the reaction of adsorbed nitrogen with hydrogen. Burch et al. [25] suggested a mechanism for NO_x reduction, which involves the dissociation of NO on a reduced surface to give adsorbed $N_{(ads)}$ and $O_{(ads)}$ with subsequent desorption of N_2 and N_2O. They believed that this mechanism could explain several reduction observations over platinum group metal catalysts for some reducing agents.

Some mathematical models describing the NSR process are presented in the literature and most of them are global kinetic models. Olsson et al. [26,27] and Tuttlies et al. [28] describe the mass transport in their respective kinetic models by a shrinking core model [26–28]. The NO_x storage over Pt/Ba/Al is described over one type of storage site and the reducing agents used in these models were CO or C_3H_6. In a recent publication by Scholz et al. [29] a global reaction kinetic model based on a multiple storage site mechanism have been presented. Hydrogen was used as the reducing agent and ammonia formation was observed in some of the experiments used to develop the model. However, the NH_3 formation was not included in the model. The reaction mechanisms in the above mentioned models are simplified and contain global reaction steps.

Laurent et al. [30] developed a more detailed model with elementary reaction steps describing the NO oxidation. However, the reactions describing the adsorption and desorption of NO_x were global reaction steps and the reduction was not modeled. The most detailed model of NO_x storage and reduction over a Pt/Ba/Al catalyst have been presented by Olsson et al. [7,8]. The first step in the proposed mechanism is NO oxidation to NO_2 over Pt. Nitrogen dioxide is then adsorbed on barium to form BaO–NO_2, which is subsequently converted into barium nitrate and NO is simultaneously released. A reversible spillover step of NO_2 between Pt and BaO sites is also included in the model. The model could describe NO_x storage and regeneration with propene between 300 and 500 °C. The model was developed with experiments without CO_2 and H_2O present in the gas feed [7,8].

To summarize: several mechanistic investigations of the NO_x storage and reduction process under various conditions have been performed and detailed descriptions particularly of the storage period have been proposed. However, very few of the mechanisms presented in the literature have been examined and verified by detailed kinetic models. There are today no detailed kinetic models that describe the storage and regeneration with hydrogen, including ammonia formation. In addition, no detailed models are available that consider experiments with high concentrations of CO_2 and H_2O, which is the case in real applications. In this study a detailed kinetic model of NO_x storage and reduction, in the presence of H_2O and CO_2, with hydrogen as the reducing agent was developed and validated. The ammonia formation in the rich period is simulated and both long and short cycles were used in the model development. The understanding gained from an extensive experimental study over the same Pt/Ba/Al catalyst [31] is used to develop this model, together with our detailed kinetic model of NO_x reduction with hydrogen over Pt/Si [32] and the NO oxidation model from Olsson et al. [7]. In addition the mechanism of NO_x storage is based on the detailed kinetic model by Olsson et al. [7].

2. Experimental

2.1. Catalyst sample

A Pt/Ba/Al monolith sample with a cell density of 400 cpsi was examined in this study. The length of the catalyst is 30 mm. It has a diameter of 21 mm and the channels are about 1 × 1 mm. The catalyst was prepared by first washcoating a cordierite monolith with γ-alumina, which was followed by incipient wetness impregnation of platinum. Barium was added to the sample after the Pt impregnation. The Pt precursor used was $Pt(NO_3)_2$ and the precursor for barium was $Ba(NO_3)_2$. The preparation method used in the work is described in detail in [31]. The washcoat weight of the sample is 1040 mg and it contains 2.9 wt% Pt and 20.8 wt% Ba. The specific surface area of the sample, which was determined by nitrogen adsorption at 77 K according to the BET method, is 97 $m^2/g_{washcoat}$. The instrument used for this purpose was a Micromeritics ASAP 2010. The Pt dispersion is 18% and was determined by N_2O dissociation in a reactor equipped with a mass spectrometer (Balzer QME 125) [33].

2.2. Reactor experiments

The experiments conducted in this study were performed in a flow reactor consisting of a horizontal quartz tube where the catalyst is placed. A total flow rate of 3500 ml/min (SV = 20 210 h^{-1}) was used in all experiments. All gases, except H_2O, were introduced into a gas blender via several mass flow controllers. Water was added to the gas flow downstream of the blender in an evaporator, which was heated to 150 °C. By exerting pressure on a container holding the water the amount of H_2O was controlled. The gas flow was fed into the reactor downstream of the evaporator. Argon was used as the carrier gas in all of the measurements. Two thermocouples were used to measure and control the temperature; one thermocouple was placed about 10 mm in front of the catalyst and the other was placed inside the catalyst, 10 mm from the rear end. An insulated heating wire was used to heat the reactor. The outlet gases were analyzed by a chemiluminescence NO_x detector (CLD 700) and by a gas FTIR (Bio-Rad FTS 3000 Excalibur Spectrometer with a Specac Sirocco series heatable gas cell, P/N 24102, with a 2 m path length and a volume of 0.19 l).

Prior to all experiments the sample was pretreated at 500 °C; first it was oxidized in 8% O_2 for 10 min, this was followed by 5 min of 100% Ar and finally the sample was reduced in 1.8% H_2 for 10 min. Five transient NO_x storage and reduction experiments were used when developing the model. Two cycling experiments with a lean period of 600 s and a rich period of 300 s were performed at 300 and 400 °C. The catalyst was exposed to 300 ppm NO, 8% O_2, 3% H_2O and 3% CO_2 during the lean period and to 300 ppm NO,

8000 ppm H_2, 3% H_2O and 3% CO_2 during the rich period in these experiments.

In addition, three lean/rich cycling experiments, with a 210 s long lean period and a 15 s long rich period were conducted at 200, 300 and 400 °C. The catalyst was exposed to 300 ppm NO, 8% O_2, 3% H_2O and 3% CO_2 during the lean periods and to 300 ppm NO, 16 000 ppm H_2, 3% H_2O and 3% CO_2 during the rich periods.

Experiments with shorter lean/rich (60 s/15 s) periods were also conducted and these experiments were used to validate the model. The gas feed in the model validation experiments were 300 ppm NO, 8% O_2, 3% H_2O and 3% CO_2 during the lean period and 300 ppm NO, 16 000 ppm H_2, 3% H_2O and 3% CO_2 during the rich period.

3. Modeling of reaction kinetics

3.1. Reactor model

The catalyst is described as a series of continuously stirred tank reactors (CSTR). The theoretical number of tanks can be estimated by using the dispersion model in combination with the tanks-in-series model [34], which considers the axial dispersion. This results in about 40 elements. However, the simulation time would be very long when using 40 elements. In addition, the effect of changing the number of tanks is most pronounced when using few tanks. Westerberg et al. [35] used ten elements in their simulation of HC SCR instead of the theoretical 40–140 in their case and estimated that the error when doing this was less than 3%. We also chose to use ten elements in our simulations, which also was done for NO reduction over Pt/SiO_2 [32] and NO_x storage with propene regeneration [8].

The assumptions made for the reactor model are:

(i) Uniform radial flow distribution.
(ii) No radial concentration gradients.
(iii) No axial diffusion, dispersion is accounted for by the number of tanks in series.
(iv) No gas phase accumulation.
(v) No diffusion resistance in the washcoat.
(vi) The average coverage of the surface, in each tank, is used to model the surface reactions.
(vii) No energy balance is solved. The temperature gradients were small when switching from lean to rich. In the switch the catalyst temperature changed less than 10 °C for all short cycles and about 12 °C for the long cycle at 400 °C and 20 °C at 300 °C. The reason for the small temperature differences is heat losses in the reactor system. Further, the temperature measured in the catalyst was used in all simulations.

The mass balance for the gas in each tank is

$$F_{i,k-1} - F_{i,k} - k_{c,i,k} \cdot A_k \cdot (c_{g,i,k} - c_{s,i,k}) = 0, \tag{1}$$

where the net molar flow from tank k, is balanced by the mass transport from the gas bulk to the catalyst surface. The nomenclature is shown in Appendix A. The mass transport to the catalyst is balanced by adsorption on, desorption from, and reaction on, the catalyst surface

$$k_{c,i,k} \cdot A_k \cdot (c_{g,i,k} - c_{s,i,k}) = \sum_j \upsilon_{i,j} \cdot r_{j,k} \cdot m_{wc,k}. \tag{2}$$

Accumulation on the surface is balanced by the sum of all reactions for each species

$$N_{cat} \frac{\partial \theta_{i,k}}{\partial t} = \sum_j \upsilon_{i,j} \cdot r_{j,k}. \tag{3}$$

The mass transfer is described by the film model, which assumes that the transport resistance (to and from the catalyst surface) is concentrated to a stagnant film layer. The mass transfer coefficient decreases from the channel inlet. The expression used for the Sherwood number is from Ref. [36]

$$\mathrm{Sh} = \mathrm{Sh}_\infty + 6.874 \cdot (1000 \cdot z_m)^{-0.488} \cdot e^{-57.2 z_m}, \tag{4}$$

where Sh_∞ is the asymptotic Sherwood number which is set to 3.0 in the model, and z_m is the dimensionless axial distance for the mass transfer, as given by this equation

$$z_m = \frac{z}{d \cdot \mathrm{Re} \cdot \mathrm{Sc}} = \frac{z \cdot D}{d^2 \cdot v}. \tag{5}$$

The Sherwood number is used to calculate the mass transfer coefficient, $k_{c,i,k}$

$$\mathrm{Sh} = \frac{k_{c,i,k} \cdot d}{D}, \tag{6}$$

where the diffusivity is calculated using

$$D = D_{ref} \left(\frac{T_f}{T_{ref}} \right)^{1.75}. \tag{7}$$

The reference temperature was 673 K and the diffusion coefficients were calculated from an equation given by Fuller et al. [37], resulting in 9.71×10^{-5} for NO, 7.51×10^{-5} for NO_2, 8.31×10^{-5} for O_2, 34.12×10^{-5} for H_2, 9.35×10^{-5} for NH_3, 10.68×10^{-5} for H_2O, 8.27×10^{-5} for N_2 and 6.43×10^{-5} m^2/s for CO_2.

3.2. Kinetic model

3.2.1. Parameters in the kinetic model

The rate constants in the kinetic model are described by the Arrhenius expression,

$$k_j = A_j \cdot e^{-E_{aj}/(R \cdot T)}, \tag{8}$$

and the pre-exponential factors and activation energies for all reactions used in the model are listed in Tables 5, 7, 9, and 11. To decrease the correlation between parameters in reactions where both the pre-exponential factor and the activation energy were fitted, a centered expression was used to describe the rate constant

$$k_j = A_j e^{(-E_{aj}/R)[(1/T)-(1/T_{ref})]}. \tag{9}$$

Several parameters were kept constant in the modeling. Adsorption reactions are usually non-activated and many of the activation energies for adsorption are therefore set to 0 kJ/mol. The pre-exponential factors for adsorption reactions, A_{ads}, in the NO oxidation and NO_x reduction sub-models were determined by using kinetic gas theory [38]

$$A_{ads} = \frac{N_A \cdot R \cdot T}{(2 \cdot \pi \cdot M \cdot R \cdot T)^{1/2}} A \cdot N_{cat} \cdot S(0). \tag{10}$$

The temperature dependence of the pre-exponential factors was neglected and a reference temperature of 573 K was used in Eq. (10). In addition, literature values were used to keep some parameters at a constant value. According to transition state theory the pre-exponential factors for reactions and desorption are within the range of 10^{11}–10^{19} s^{-1} [38]; usually 10^{13} s^{-1} is used due to

$$\frac{k_B \cdot T}{h} = 10^{13}\ s^{-1}. \tag{11}$$

Hence, several of the pre-exponential factors used in the model were set to 10^{13} s^{-1}.

The thermodynamics for gas phase equilibrium reactions must always be fulfilled. Thermodynamic constraints are therefore put on the gas phase reactions in the model.

Statistical thermodynamics [38] was used to confirm that the pre-exponential factors for the adsorption and desorption reactions are reasonable. This is done by calculating the change in entropy for a gas phase species that adsorbs on the catalyst surface,

$$\Delta S_{\text{model}} = R \ln \frac{A_{\text{ads}}}{A_{\text{des}}}. \tag{12}$$

A realistic value of the change in entropy lies in the range between two extreme cases: the change in entropy for a completely localized adsorbate (ΔS_{loc}) and an adsorbed specie behaving as a 2D gas (ΔS_{2D}). These entropy changes are given by [7]

$$\Delta S_{\text{loc}} = S_{\text{tr,3D}} + S_{\text{rot,3D}}, \tag{13}$$

$$\Delta S_{2D} = S_{\text{tr,3D}} + S_{\text{rot,3D}} - (S_{\text{tr,2D}} + S_{\text{rot,2D}}). \tag{14}$$

The entropies are calculated from

$$S = R \ln(q) + RT \frac{d(\ln(q))}{dT}, \tag{15}$$

where the partition functions for translation in two and three dimensions and the partition function for rotation for linear and non-linear (symmetric and asymmetric) molecules are calculated as follows [39]

$$q_{\text{tr,3D}} = \frac{(2\pi m k_B T)^{3/2}}{h^3} V, \tag{16}$$

$$q_{\text{tr,2D}} = \frac{2\pi m k_B T}{h^2} A, \tag{17}$$

$$q_{\text{rot}} = \frac{8\pi^2 I_x k_B T}{\sigma_r h^2} \quad \text{(linear)}, \tag{18}$$

$$q_{\text{rot}} = \frac{\pi^{1/2}}{\sigma_r} \frac{(8\pi^2 I_x k_B T)}{h^2} \frac{(8\pi^2 I_z k_B T)^{1/2}}{h^2} \quad \text{(symmetric, non-linear)}, \tag{19}$$

$$q_{\text{rot}} = \frac{\pi^{1/2}}{\sigma_r} \frac{(8\pi^2 I_x k_B T)^{1/2}}{h^2} \frac{(8\pi^2 I_y k_B T)^{1/2}}{h^2} \frac{(8\pi^2 I_z k_B T)^{1/2}}{h^2} \quad \text{(asymmetric, non-linear)}. \tag{20}$$

The rotational constants used for calculating the moment of inertia are from Herzberg [40]. The parameters that were not fixed by the above mentioned ways were fitted using the least-squares method and the 95% linearized confidence intervals were calculated for these parameters. Five transient experiments were used in the modeling to obtain the parameter values; a more detailed description of the parameters is presented below.

3.2.2. Mechanism

The detailed kinetic model used in this work is divided into four sub-models: (i) NO oxidation over Pt, (ii) NO_x reduction over Pt, (iii) NO_x storage and (iv) NO_x regeneration. These sub-models describe the steps occurring over Pt/Ba/Al catalysts during NO_x storage and reduction cycles with hydrogen as the reducing agent. The mechanisms of the sub-models are listed in Tables 1–4. All sub-models are used when modeling the cycling experiments presented in the results. The kinetic model was developed stepwise and a detailed description of the subsystems is presented below.

3.2.2.1. NO oxidation over Pt The sub-model used to describe NO oxidation over Pt in this work was developed by Olsson et al. [7] over a Pt/Al and a Pt/Ba/Al catalyst. The mechanism used in the modeling is presented in Table 1. The activation energy for oxygen desorption and for NO_2 desorption are dependent on the oxygen coverage on platinum, in accordance with the model in Ref. [7]. The background for this is that there are repulsive interactions between oxygen atoms on the surface. In order to have thermodynamic consistency it was also assumed that there are repulsive interactions between oxygen and NO_2. This means that in addition to the pre-exponential factors and the activation energies, two more parameters (two linear constants denoted α_4 and α_7) describe the NO oxidation system.

Table 1
Mechanism for NO oxidation

Reaction number	Reaction
1 and 2	$NO_{(g)} + Pt \underset{r_2}{\overset{r_1}{\leftrightarrow}} NO\text{–}Pt$
3 and 4	$O_{2(g)} + 2Pt \underset{r_4}{\overset{r_3}{\leftrightarrow}} 2O\text{–}Pt$
5 and 6	$NO\text{–}Pt + O\text{–}Pt \underset{r_6}{\overset{r_5}{\leftrightarrow}} NO_2\text{–}Pt + Pt$
7 and 8	$NO_2\text{–}Pt \underset{r_8}{\overset{r_7}{\leftrightarrow}} NO_{2(g)} + Pt$

Table 2
Mechanism for the NO_x storage

Reaction number	Reaction
9 and 10	$NO_{2(g)} + BaCO_3 \underset{r_{10}}{\overset{r_9}{\leftrightarrow}} NO_2\text{–}BaCO_3$
11 and 12	$NO_2\text{–}BaCO_3 \underset{r_{12}}{\overset{r_{11}}{\leftrightarrow}} BaO\text{–}NO_2 + CO_{2(g)}$
13 and 14	$NO_2\text{–}BaO + 2NO_2\text{–}Pt \underset{r_{14}}{\overset{r_{13}}{\leftrightarrow}} Ba(NO_3)_2 + 2Pt + NO_{(g)}$
15 and 16	$NO_{(g)} + BaCO_3 \underset{r_{16}}{\overset{r_{15}}{\leftrightarrow}} NO\text{–}BaCO_3$
17 and 18	$NO_{(g)} + S_3 \underset{r_{18}}{\overset{r_{17}}{\leftrightarrow}} S_3\text{–}NO$
19 and 20	$NO\text{–}S_3 + O\text{–}Pt \underset{r_{20}}{\overset{r_{19}}{\leftrightarrow}} NO_2\text{–}S_3 + Pt$
21 and 22	$NO_{2(g)} + S_3 \underset{r_{22}}{\overset{r_{21}}{\leftrightarrow}} S_3\text{–}NO_2$

3.2.2.2. NO_x storage The NO_x storage sub-model is based on the model developed by Olsson et al. [7,8] and was modified in this work due to the inclusion of high concentrations of water and CO_2 in the feed and NO_x storage at low temperature. In addition, a few reaction steps were summarized in order to decrease the number of parameters. The model is presented in Table 2. The mechanism contains seven reversible steps and NO_x is allowed to be stored at two different types of storage sites.

A previous experimental investigation of this catalyst showed that when both CO_2 and H_2O are included in the gas mixture, the negative effect on the storage capacity for this catalyst is more pronounced for CO_2 than for H_2O [31]. This was explained by the difference in stability of $BaCO_3$ and $Ba(OH)_2$ ($BaCO_3$ is more stable than $Ba(OH)_2$ [41]). Furthermore, it was shown that the storage over barium was more sensitive to CO_2 than to H_2O. Due to the above mentioned reasons it is assumed that the barium sites are in the carbonate form during the prevailing conditions (i.e. excess of CO_2 and H_2O).

In several studies it is suggested that there are different types of storage sites present in NO_x storage catalysts [13,14,20,22,41,42]. $NO + O_2$ and also NO_2 TPD experiments over Pt/Ba/Al clearly shows several desorption peaks [43]. This can be explained by either that there are different NO_x species with varying strength on the surface or that there are different types of storage sites or a combination of the two. In the literature there are different explanations for the multiple storage sites:

(i) The proximity between the noble metal and the barium, resulting in different storage sites close and far from barium [13,14,20]
(ii) Storage on barium and alumina. It is well known that NO_x can be stored on alumina at lower temperatures [31,35]. According to FTIR results by Dawody et al. [44] the barium do not cover all alumina sites. However, FTIR measurements from Labalme et al. [45] showed the opposite result with barium covering all alumina sites. The differences are likely due to differences

in preparation methods. When analyzing FTIR spectra Westerberg and Fridell [35] assigned the peaks to different nitrites and nitrates on barium, alumina and alumina in close contact with barium.

(iii) The presence of BaO, $Ba(OH)_2$ and $BaCO_3$ which have different affinity for NO_x [41].

(iv) Different adsorption strengths of NO_x on surface barium and bulk barium sites [22,42]. Scanning electron microscopy (SEM) in combination with energy dispersive X-ray spectrometry (EDS) showed the concentration of barium on the surface varied [33]. Based on TPD, IR, and ^{15}N solid state NMR Szanyi et al. [42] suggest that there is a thin monolayer of barium on the alumina and bulk barium particles formed on this layer. The surface nitrates have lower stability compared to the bulk nitrates.

Thus many studies suggest that there are multiple storage sites in the Pt/Ba/Al catalyst, but the physical explanation of them differs. We have added a second storage site in our NO_x storage model denoted S_3 (three types of sites are present in the model: Pt, $BaCO_3$ and S_3) in order to describe the experimental results, which clearly support multiple storage sites. In the NO_x storage model presented in Ref. [46] by Dawody et al. a second storage site was also introduced.

The first three reversible reactions in the NO_x storage submodel describe the storage of NO_2 over $BaCO_3$. In reaction 9 NO_2 adsorbs on $BaCO_3$ and form NO_2–$BaCO_3$. Carbon dioxide can then desorb from the formed specie and produce BaO–NO_2 (reaction 11). The NO_x storage process is very complex and several mechanisms with many reaction steps have been suggested in the literature [5,7,10]. In order to decrease the number of reactions in the model we have chosen to describe the formation of $Ba(NO_3)_2$ via a reversible spill-over step (reactions 13 and 14) with NO_2 from platinum, since previous simulations and experiments have shown that the storage of NO_x is more favored in the presence of a noble metal [7]. Furthermore, it has been shown that the proximity of Pt and Ba is very important for the NO_x storage [10,15]. Together with reactions 7 and 8, i.e. desorption and adsorption of NO_2 over Pt, the above mentioned reactions establish the disproportionation reaction, where three NO_2 molecules are consumed and one NO molecule is released, as shown below

$$3NO_{2(g)} + BaCO_3 \leftrightarrow NO_{(g)} + CO_{2(g)} + Ba(NO_3)_2.$$

As stated above, the activation energy for NO_2 desorption over Pt (E_{a8}) is dependent on the oxygen coverage on platinum. Since the enthalpy and entropy changes for the overall equilibrium reaction are not allowed to vary, one additional activation energy must be dependent on the oxygen coverage to compensate for the change in the enthalpy. The activation energy for the spill-over reaction (E_{a13}) was chosen to be coverage dependent in this model according to

$$E_{a13}(\theta) = Ea_{13}(0)(1 - \alpha_{13}\theta_{Pt\text{–}O}),$$

where α_{13} is a linear constant and $\theta_{Pt\text{–}O}$ the coverage of oxygen over platinum.

Prinetto et al. [43] exposed a Pt/Ba/Al catalyst to NO at room temperature and the resulting FTIR spectra showed NO_x species on the surface. They also conducted a NO TPD at 313 K and observed desorption of NO. The amount of stored NO_x increased significantly when exposing the catalyst to a combination of NO and O_2 and this was observed already at room temperature where the NO oxidation is usually very low [43]. This is consistent with NO + O_2 TPD experiments performed by Olsson et al. [47] where a large storage was observed at 100 °C, without any NO oxidation activity. In addition, Westerberg et al. [35] conducted in situ FTIR measurements over BaO/Al_2O_3 and Al_2O_3 and observed NO_x species on the surface after NO + O_2 exposure between 100 and 300 °C. Since these samples do not contain a noble metal the oxidation capacity can be neglected. Thus, NO can adsorb on the Pt/Ba/Al catalyst and we have therefore added adsorption and desorption of NO over $BaCO_3$ (reactions 15 and 16) and the corresponding reaction on S_3 (reactions 17 and 18) to the model. These steps were very important in order to simultaneously describe the complete uptake of NO_x in the beginning of the lean period when feeding the catalyst with NO and O_2 at 200 °C and the low NO oxidation activity.

Table 3
Mechanism for NO_x reduction

Reaction number	Reaction
23 and 24	$H_{2(g)} + 2Pt \underset{r_{24}}{\overset{r_{23}}{\leftrightarrow}} 2H\text{–}Pt$
25	$O\text{–}Pt + 2H\text{–}Pt \overset{r_{25}}{\rightarrow} H_2O\text{–}Pt + 2Pt$
26 and 27	$H_2O_{(g)} + Pt \underset{r_{27}}{\overset{r_{26}}{\leftrightarrow}} H_2O\text{–}Pt$
28 and 29	$NO\text{–}Pt + Pt \underset{r_{29}}{\overset{r_{28}}{\leftrightarrow}} N\text{–}Pt + O\text{–}Pt$
30	$2N\text{–}Pt \overset{r_{30}}{\rightarrow} N_{2(g)} + 2Pt$
31	$N\text{–}Pt + 3H\text{–}Pt \overset{r_{31}}{\rightarrow} NH_3\text{–}Pt + 3Pt$
32 and 33	$NH_{3(g)} + Pt \underset{r_{33}}{\overset{r_{32}}{\leftrightarrow}} NH_3\text{–}Pt$

Nova et al. [10] described the mechanism of NO_x storage by two routes that operate simultaneously, the nitrate route, which is adsorption of NO_2 via the disproportionation reaction, and the nitrite route. The nitrite route involves the direct uptake of NO in the presence of O_2 on the barium component, to form adsorbed nitrite species. The nitrites are then oxidized to nitrates. This alternative storage route explains the experimental findings that the presence of oxygen increases the storage of NO, without NO oxidation occurring on the platinum [35,47]. A similar route is used in the mechanism for NO_x storage applied in this study; NO adsorbed over S_3 can be further oxidized to NO_2 by reacting with oxygen on neighboring Pt sites according to reaction 19. Reaction 19 is reversible and NO_2 dissociation is described by reaction 20. Adsorption and desorption of NO_2 over S_3 is also included in the model according to reactions 21 and 22. By introducing the reversible reaction of NO oxidation over S_3, there is a second possible route for NO oxidation in the model proposed here. This route occurs over Pt and S_3 and contains r_3, r_4, r_{17}, r_{18}, r_{19}, r_{20}, r_{21} and r_{22}. Also for this route one additional activation energy, besides the activation energy for oxygen desorption (E_{a4}), must be dependent on the oxygen coverage. The activation energy of the forward spill-over reaction (E_{a19}) was chosen to compensate for the change in the enthalpy:

$$E_{a19}(\theta) = E_{a19}(0)(1 - \alpha_{19}\theta_{Pt\text{–}O}).$$

Also here is α_{19} the linear constant and $\theta_{Pt\text{–}O}$ the coverage of oxygen over platinum.

3.2.2.3. NO_x reduction over Pt The reduction of NO_x to nitrogen occurs over the precious metal of a NSR catalyst. Experimental investigations have shown that NH_3 and N_2O are common byproducts when reducing NO_x with hydrogen over Pt [21,32]. A model describing NO_x reduction over Pt was constructed over a Pt/Si catalyst [32] and this model was used in this work to explain the reduction of NO_x and the formation of NH_3 over Pt. The mechanism used here is presented in Table 3. Nitrous oxide production was not included in this model, since N_2O was not measured in this work.

Hydrogen is a very effective reductant for NSR catalysts. In this model hydrogen cleans the surface from oxygen adsorbed on Pt by producing H_2O according to reaction 25. Earlier studies have shown that H_2O inhibits the NO oxidation capacity of the

Table 4
Mechanism for NO_x regeneration

Reaction number	Reaction
34	$6H–Pt + Ba(NO_3)_2 + CO_{2(g)} \xrightarrow{r_{34}} 2NO–Pt + BaCO_3 + 3H_2O–Pt + Pt$
35	$4H–Pt + BaO–NO_2 + CO_{2(g)} \xrightarrow{r_{35}} 0.5N_{2(g)} + BaCO_3 + 2H_2O–Pt + 2Pt$
36	$4H–Pt + 2BaCO_3–NO \xrightarrow{r_{36}} N_{2(g)} + 2BaCO_3 + 2H_2O–Pt + 2Pt$
37	$2H–Pt + NO_2–S_3 \xrightarrow{r_{37}} NO–Pt + S_3 + H_2O–Pt$
38	$4H–Pt + 2NO–S_3 \xrightarrow{r_{38}} N_{2(g)} + 2S_3 + 2H_2O–Pt + 2Pt$
39	$2NH_3–Pt + 3O–Pt \xrightarrow{r_{39}} N_{2(g)} + 3H_2O_{(g)} + 5Pt$
40	$2NH_3–Pt + Ba(NO_3)_2 + Pt \xrightarrow{r_{40}} 1.5N_{2(g)} + BaO–NO_2 + 3H_2O–Pt$
41	$4NH_3–Pt + 3NO_2–BaO + 2Pt + 3CO_{2(g)} \xrightarrow{r_{41}} 3.5N_{2(g)} + 3BaCO_3 + 6H_2O–Pt$

catalyst [48], which may be due to blocking of Pt sites. In this model adsorption and desorption of H_2O is included (reactions 26 and 27). Reaction 25 results in vacant Pt sites which are needed for NO dissociation (reaction 28). Nitrogen adsorbed on Pt can then further react and form N_2 (reaction 30) and NH_3 (reaction 31). Ammonia adsorption and desorption are described by reactions 32 and 33.

3.2.2.4. NO_x regeneration Table 4 presents the reactions describing the regeneration of NO_x that were used in this model. The introduction of a reducing agent increases the rate of regeneration of the storage sites in NO_x storage and reduction catalysts. The reduction of NO_x occurs over the noble metal sites. Hence, the NO_x adsorbed must either desorb from the storage sites into the gas phase and readsorb on the precious metal or it must diffuse over the surface to the precious metal. However, the desorption rates of the nitrites and nitrates are low and it is therefore not possible to describe the regeneration of the adsorbed species using reactions on the noble metal only. We have previously described the importance of spill-over of NO_x in the storage and release process using detailed kinetic simulations [7]. Further, previous studies have emphasized the importance of the proximity of Pt and Ba for NO_x decomposition [24,49,50]. In addition, ab initio molecular dynamics simulations have shown that both nitrites and nitrates can diffuse on BaO(100) [51]. We therefore propose that the regeneration occurs through a reaction with hydrogen adsorbed on platinum and the stored NO_x, via a spill-over mechanism.

The reaction between the stored NO_x and hydrogen results in a regeneration of the storage sites and a simultaneous production of N_2. However, experimentally it is well known that all NO_x is not reduced to N_2 during the rich period, and a NO_x release peak is often observed. Thus, the stored NO_x reacts with the hydrogen and produces both N_2 and NO. We have therefore added reaction steps for the regeneration of the stored NO_x to form NO on Pt or N_2. In our model there are four NO_x species on the Ba sites ($BaO–NO_2$, $Ba(NO_3)_2$, $NO–BaCO_3$, $NO_2–BaCO_3$) and two on the S_3 sites ($NO–S_3$, $NO_2–S_3$). However, $NO_2–BaCO_3$ is an intermediate, which always has a very low coverage and regeneration steps are therefore not needed for this specie. To put up detailed reaction schemes for the regeneration of the five NO_x storage species would require very many reaction steps and the parameters would be so highly correlated that it would not be possible to resolve. We have therefore used summary step to decrease the number of parameters. In the mechanism the most strongly bound NO_x species on both storage sites ($Ba(NO_3)_2$ and $NO_2–S_3$) reacts to produce NO on Pt and the other species forms N_2 directly. These set of reactions 34–38 is the smallest amount of reactions needed to describe the regeneration, since only one reaction step is added for the regeneration of each of the five stored NO_x species.

It is well known that ammonia is easily oxidized into N_2 in NH_3 SCR systems [52] and it can also occur at high temperatures in the gas phase [53]. Ammonia oxidation can also occur over Pt and this is therefore included in the model (reaction 39). The experimental study performed over this catalyst showed that when switching to rich conditions there is a delay of about two min before NH_3 is observed [31]. This delay is dependent on the H_2 concentration, when increasing the H_2 concentration the delay time is shortened [31]. However, in the end of the rich period the selectivity of NO reacting to produce ammonia is about 100%. Thus, the rate for ammonia production must be very high. When starting the rich period there is a large NO peak observed due to decomposition of nitrates, but at the same time there is no ammonia seen. The ammonia first starts to break through when the NO signal is close to zero. In order to describe these experimental features, i.e. a very high rate for ammonia production but no ammonia observed in the initial part of the rich period, we propose that the nitrites/nitrates adsorbed on the storage components react with ammonia and produce N_2 and H_2O according to SCR chemistry. When the nitrites and nitrates are depleted ammonia is observed in the gas phase. This is consistent with the experimental findings and is described by summary reactions (reactions 40 and 41) in the model, where barium nitrate and $BaO–NO_2$, respectively, react with NH_3 adsorbed on Pt. These two steps were critical in order to describe the ammonia production in the rich period properly. It is also possible that other NO_x species on the surface can react with ammonia. However, these two steps were the most critical and we wanted to minimize the number of reactions in the model.

Table 5
Reaction rates and kinetic parameters for NO oxidation

No.	Reaction rate	Pre-exponential factor	Ref.	Activation energy (kJ/mol)	Ref.
1.	$r_1 = k_1 \cdot c_{NO_{(g)}} \cdot \theta_{v,Pt}$	5.8×10^3 [a]	[7]	0	[7]
2.	$r_2 = k_2 \cdot \theta_{Pt–NO}$	1.0×10^{16} [b]	[7]	108.5	[32]
3.	$r_3 = k_3 \cdot c_{O_{2(g)}} \cdot \theta_{v,Pt}^2$	1.4×10^2 [a]	[7]	20.4	[32]
4.	$r_4 = k_4 \cdot \theta_{Pt–O}^2$	1.0×10^{15} [b]	[7]	199.4 [d,e]	
5.	$r_5 = k_5 \cdot \theta_{Pt–NO} \cdot \theta_{Pt–O}$	$5.5 \times 10^1 \pm 0.7 \times 10^1$ [c,f]		142.3 ± 9.3 [c]	
6.	$r_6 = k_6 \cdot \theta_{Pt–NO_2} \cdot \theta_{v,Pt}$	5.5×10^{14} [b,d]		100.5 [a]	
7.	$r_7 = k_7 \cdot \theta_{Pt–NO_2}$	1.0×10^{16} [b]	[7]	97.9	[7]
8.	$r_8 = k_8 \cdot c_{NO_{2(g)}} \cdot \theta_{v,Pt}$	5.2×10^3 [a]	[7]	0	[7]

[a] Unit: $m^3/(s\ kg\ of\ washcoat)$.
[b] Unit: s^{-1}.
[c] Parameter fitted in this work.
[d] Calculated from thermodynamic restrictions [7].
[e] The activation energy is dependent on the oxygen coverage, i.e. $E_i(\theta) = E_i(0) \cdot (1 - \alpha_i \cdot \theta_{Pt–O})$. $\alpha_4 = 0.116$ and $\alpha_7 = 0.118$.
[f] Centered value. Unit: mol/(s kg of washcoat).

4. Results and discussion

4.1. Parameters for the NO oxidation over Pt

The results from five experiments are used in the modeling to obtain the parameters for all sub-models. Table 5 presents the reaction rates and the kinetic parameters in the NO oxidation submodel. Nine of the parameters are from Olsson et al. [7] and two of them, the activation energy of NO desorption (E_{a2}) and oxygen adsorption (E_{a3}), are from Ref. [32]. Five parameters were calculated from thermodynamic restrictions (E_{a4}, α_4, A_6, E_{a6} and α_7) and only two parameters out of 18 were fitted. The number of Pt sites is 2.7×10^2 mol/(kg of washcoat), which was obtained from the Pt dispersion measurement conducted over this catalyst.

The pre-exponential factors for adsorption were taken from [7], as described above. They are derived from Eq. (10) using the sticking coefficient. For oxygen adsorption the sticking is 0.023 over Pt(111) at 600 K according to Elg et al. [54], and this value is used in the present study and also [7]. For NO is the sticking coefficient 0.87 on Pt(110) and 0.9 on Pt(111) [55] and we have therefore used $S_{0(NO)} = 0.9$ [7]. For NO_2 the value reported by Bartram et al. [56] is close to unity (0.97) and we have therefore used $S_{0(NO_2)} = 1$ [7].

Table 6
Entropy changes for the adsorption and desorption reactions in the NO oxidation submodel, a 2D gas and a localized adsorbate

Reaction	ΔS_{2D} (J/(mol K)	ΔS_{loc} (J/(mol K)	ΔS_{model} (J/(mol K)
$NO_{(g)} + Pt \leftrightarrow NO\text{–}Pt$	−99	−215	−180
$O_{2(g)} + 2Pt \leftrightarrow 2O\text{–}Pt$	−101	−211	−192
$NO_{2(g)} + Pt \leftrightarrow NO_2\text{–}Pt$	−101	−252	−181

Table 7
Reaction rates and kinetic parameters for the NO_x storage submodel

No.	Reaction rate	Pre-exponential factor	Activation energy (kJ/mol)	Ref.
9.	$r_9 = k_9 \cdot c_{NO_{2(g)}} \cdot \theta_{v,BaCO_3}$	$4.0 \times 10^2 \pm 0.5 \times 10^{2}$ [a,b]	27.9	[7]
10.	$r_{10} = k_{10} \cdot \theta_{BaCO_3\text{–}NO_2}$	8.7×10^{13} [c]	186.4	[7]
11.	$r_{11} = k_{11} \cdot \theta_{BaCO_3\text{–}NO_2}$	1.8×10^{13} [c]	82.8 ± 54.1 [b]	
12.	$r_{12} = k_{12} \cdot c_{CO_{2(g)}} \cdot \theta_{BaO\text{–}NO_2}$	4.0×10^{2} [a]	0	
13.	$r_{13} = k_{13} \cdot \theta_{BaO\text{–}NO_2} \cdot \theta_{Pt\text{–}NO_2}$	1.0×10^{13} [c]	114.5 ± 0.4 [b,e]	
14.	$r_{14} = k_{14} \cdot \theta_{Ba(NO_3)_2} \cdot \theta_{v,Pt} \cdot c_{NO_{(g)}}$	3.9×10^{-4} [c,d]	12.4 [d]	
15.	$r_{15} = k_{15} \cdot c_{NO_{(g)}} \cdot \theta_{v,BaCO_3}$	4.7×10^{2} [a]	33.2 ± 0.3 [b]	
16.	$r_{16} = k_{16} \cdot \theta_{BaCO_3\text{–}NO}$	1.0×10^{13} [c]	158.4 ± 2.0 [b]	
17.	$r_{17} = k_{17} \cdot c_{NO_{(g)}} \cdot \theta_{v,S_3}$	$1.4 \times 10^2 \pm 0.3 \times 10^{2}$ [a,b]	0	
18.	$r_{18} = k_{18} \cdot \theta_{S_3\text{–}NO}$	2.3×10^{12} [c]	106.4 ± 1.0 [b]	
19.	$r_{19} = k_{19} \cdot \theta_{S_3\text{–}NO} \cdot \theta_{Pt\text{–}O}$	1.0×10^{13} [c]	143.1 ± 0.4 [b,e]	
20.	$r_{20} = k_{20} \cdot \theta_{S_3\text{–}NO_2} \cdot \theta_{v,Pt}$	1.1×10^{13} [c,d]	156.6 [d]	
21.	$r_{21} = k_{21} \cdot c_{NO_{2(g)}} \cdot \theta_{v,S_3}$	4.3 ± 0.4 [a,b]	0	
22.	$r_{22} = k_{22} \cdot \theta_{S_3\text{–}NO_2}$	7.7×10^{11} [c]	151.1 ± 0.4 [b]	

[a] Unit: $m^3/(s\ kg\ of\ washcoat)$.
[b] Parameter fitted in this work.
[c] Unit: s^{-1}.
[d] Calculated from thermodynamic restrictions.
[e] The activation energy is dependent on the oxygen coverage, i.e. $E_i(\theta) = E_i(0) \cdot (1 - \alpha_i \cdot \theta_{Pt-O})$. $\alpha_{13} = 0.201$ and $\alpha_{14} = 0.081$.

Table 8
Entropy changes for the adsorption and desorption reactions in the NO_x storage submodel, a 2D gas and a localized adsorbate

Reaction	ΔS_{2D} (J/(mol K))	ΔS_{loc} (J/(mol K))	ΔS_{model} (J/(mol K))
$NO_{2(g)} + BaCO_3 \leftrightarrow NO_2\text{–}BaCO_3$	−90	−252	−171
$CO_{2(g)} + BaO\text{–}NO_2 \leftrightarrow NO_2\text{–}BaCO_3$	−90	−226	−158
$NO_{(g)} + BaCO_3 \leftrightarrow NO\text{–}BaCO_3$	−88	−215	−152
$NO_{2(g)} + S_3 \leftrightarrow S_3\text{–}NO_2$	−92	−252	−172
$NO_{(g)} + S_3 \leftrightarrow S_3\text{–}NO$	−90	−215	−152

The change in entropy for the reversible adsorption and desorption reactions was calculated and compared to the change in entropy for a localized adsorbate and a 2D gas. The results are presented in Table 6 and they show that the ΔS for the model are within the expected range.

4.2. Parameters for the NO_x storage

Table 7 shows the reaction rates and kinetic parameters that were used in the NO_x storage sub-model. Density functional theory (DFT) calculations on NO_x adsorption over barium have shown that NO_x is mobile on the barium surface [51]. It is therefore assumed that the entropy changes of the adsorption and desorption reactions in the model (ΔS_{model}) is between the entropy changes for a 2D gas and a localized specie. In order to fix some of the pre-exponential factors in the NO_x storage subsystem the entropy changes of the adsorption and desorption reactions in the model (ΔS_{model}) were set to the mean value of the entropy changes for a 2D gas and a localized specie. Five pre-exponential factors (A_{10}, A_{11}, A_{15}, A_{18} and A_{22}) could therefore be determined.

Table 8 presents ΔS_{2D}, ΔS_{loc} and ΔS_{model} for all adsorption and desorption reactions in the NO_x storage sub-model. The results presented in the table show that all entropy changes for these reactions are within the expected range. The pre-exponential factors for reactions 13, 16 and 19 were held constant at 10^{13} s^{-1} according to transition state theory [38] and the pre-exponential factors for reactions 14 and 20 were calculated from thermodynamic constraints. The pre-exponential factor for adsorption of CO_2 over BaO–NO_2 (A_{12}) is set to the same value as the pre-exponential factor for adsorption of NO_2 over $BaCO_3$ (A_9), since it is assumed that CO_2 adsorbs in a similar way as NO_2. In addition, the adsorption of NO_2 over $BaCO_3$ is assumed to behave similar to adsorption of NO_2 over BaO. It is therefore possible to use the same activation energies for reactions 9 and 10 in this model as in Ref. [7] for NO_2 adsorption over BaO. Hence, E_{a9} was set to 27.9 kJ/mol and E_{a10} to 186.4 kJ/mol. However, it was not possible to use the same activation energy for CO_2 adsorption over BaO–NO_2 and E_{a12} was therefore fitted. It is assumed that the other adsorption reactions (reactions 12, 17 and 21) in the model are non-activated and E_{a12}, E_{a17}, and E_{a21} are therefore fixed to 0 kJ/mol.

In the same way as for the pre-exponential factors for reactions 14 and 20, the activation energies for these reactions are calculated from thermodynamic constraints. In addition, thermodynamic restrictions determine the linear constants (α_{13} and α_{19}) in the coverage dependence of E_{a13} and E_{a19}. The NO_x storage submodel contains 30 parameters and only ten of them were fitted. These parameters are presented together with the 95% linearized confidence interval in Table 7. Moreover, Table 12 presents the number of active sites used in the model. The numbers of storage sites were fitted, which resulted in $7.1 \times 10^{-2} \pm 0.14 \times 10^{-2}$ mol/kg of washcoat for $BaCO_3$ and $10.1 \times 10^{-2} \pm 0.28 \times 10^{-2}$ mol/kg of washcoat for S_3.

Table 9
Reaction rates and kinetic parameters for NO_x reduction over Pt

No.	Reaction rate	Pre-exponential factor	Ref.	Activation energy (kJ/mol)	Ref.
23.	$r_{23} = k_{23} \cdot c_{H_{2(g)}} \cdot \theta^2_{v,Pt}$	1.2×10^3 [a]	[32]	0	[32]
24.	$r_{24} = k_{24} \cdot \theta^2_{Pt\text{–}H}$	1.0×10^{13} [b]		69.4 ± 0.9 [c]	
25.	$r_{25} = k_{25} \cdot \theta_{Pt\text{–}O} \cdot \theta^2_{Pt\text{–}H}$	1.0×10^{13} [b]		54.4	[32]
26.	$r_{26} = k_{26} \cdot c_{H_2O_{(g)}} \cdot \theta_{v,Pt}$	$K_{eq} = 1.8 \times 10^{-5}$		0	
27.	$r_{27} = k_{27} \cdot \theta_{Pt\text{–}H_2O}$			65.0	[57]
28.	$r_{28} = k_{28} \cdot \theta_{Pt\text{–}NO} \cdot \theta_{v,Pt}$	1.0×10^{13} [b]		93.0	[32]
29.	$r_{29} = k_{29} \cdot \theta_{Pt\text{–}N} \cdot \theta_{Pt\text{–}O}$	1.0×10^{13} [b]		68.2	[32]
30.	$r_{30} = k_{30} \cdot \theta^2_{Pt\text{–}N}$	1.0×10^{13} [b]		79.5	[32]
31.	$r_{31} = k_{31} \cdot \theta_{Pt\text{–}N} \cdot \theta_{Pt\text{–}H}$	1.0×10^{13} [b]		78.6	[32]
32.	$r_{32} = k_{32} \cdot c_{NH_{3(g)}} \cdot \theta_{v,Pt}$	7.7×10^3 [a]	[32]	0	[32]
33.	$r_{33} = k_{33} \cdot \theta_{Pt\text{–}NH_3}$	1.0×10^{13} [b]		87.1 ± 1.0 [c]	

[a] Unit: $m^3/(s\ kg\ of\ washcoat)$.
[b] Unit: s^{-1}.
[c] Parameter fitted in this work.

4.3. Parameters for the NO_x reduction over Pt

The reaction rates and kinetic parameters of NO_x reduction over Pt are given in Table 9. Most of the parameters are taken from Ref. [32]. The pre-exponential factors of reactions 24, 25, 28–31, and 33 were set to 10^{13} s^{-1}. The activation energy of H_2O adsorption on Pt is reported to be non-activated [57] with a sticking coefficient of 0.7 for H_2O adsorption on Pt [58]. This gives a very high reaction rate for the adsorption of H_2O. Furthermore, the reaction for H_2O desorption from Pt is very fast when using the kinetic parameters reported in the literature. Fisher et al. [57] conducted temperature programmed desorption experiments and determined the activation energy for H_2O desorption from Pt to 65 kJ/mol. The pre-exponential factor used in the simulations of NO_x reduction over Pt/Si was set to 10^{16} s^{-1} [32]. Simulations performed in this study showed that the coverage of H_2O on Pt is close to zero.

Table 10
Entropy changes for the adsorption and desorption reactions in the NO_x reduction submodel, a 2D gas and a localized adsorbate

Reaction	ΔS_{2D} (J/(mol K))	ΔS_{loc} (J/(mol K))	ΔS_{model} (J/(mol K))
$H_{2(g)} + 2Pt \leftrightarrow 2H\text{–}Pt$	−81	−146	−136
$NH_{3(g)} + Pt \leftrightarrow NH_3\text{–}Pt$	−97	−211	−192
$H_2O_{(g)} + Pt \leftrightarrow H_2O\text{–}Pt$	−97	−207	−183

Table 11
Reaction rates and kinetic parameters for NO_x regeneration

No.	Reaction rate	Pre-exponential factor	Activation energy (kJ/mol)
34.	$r_{34} = k_{34} \cdot \theta_{Pt-H} \cdot \theta_{Ba(NO_3)_2}$	0.35 ± 0.04[a,b]	56.7 ± 4.8[a]
35.	$r_{35} = k_{35} \cdot \theta_{Pt-H} \cdot \theta_{BaO-NO_2}$	0.13 ± 0.09[a,b]	62.2 ± 29.7[a]
36.	$r_{36} = k_{36} \cdot \theta_{Pt-H} \cdot \theta_{BaCO_3-NO}$	0.14 ± 0.08[a,b]	92.0 ± 114.1[a]
37.	$r_{37} = k_{37} \cdot \theta_{Pt-H} \cdot \theta_{S_3-NO_2}$	1.1×10^6[c]	56.7
38.	$r_{38} = k_{38} \cdot \theta_{Pt-H} \cdot \theta_{S_3-NO}$	7.4×10^{10}[c]	92.0
39.	$r_{39} = k_{39} \cdot \theta_{Pt-NH_3} \cdot \theta_{Pt-O}$	1.0×10^{13}[c]	114.4 ± 4.9[a]
40.	$r_{40} = k_{40} \cdot \theta_{Pt-NH_3} \cdot \theta_{Ba(NO_3)_2} \cdot \theta_{v,Pt}$	1.0×10^{13}[c]	129.0 ± 2.0[a]
41.	$r_{41} = k_{41} \cdot \theta_{Pt-NH_3} \cdot \theta_{BaO-NO_2} \cdot \theta_{v,Pt}$	0.01 ± 0.02[a,b]	74.0 ± 101.3[a]

[a] Parameter fitted in this work.
[b] Centered value. Unit: mol/(s kg of washcoat).
[c] Unit: s^{-1}.

Due to the high reaction rates and the very low coverage, it is assumed that adsorption and desorption of H_2O (reactions 26 and 27) are in equilibrium and the equilibrium constant,

$$K_{eq} = \frac{k_{26}}{k_{27}},$$

is used as parameter for this reaction. The equilibrium constant was calculated from the above mentioned parameters found in the literature.

The pre-exponential factors for adsorption of hydrogen and NH_3 were calculated using the sticking coefficients of 0.046 and 0.9, respectively, which was used in our earlier model describing NO_x reduction on Pt/SiO_2. $S_{0(H_2)} = 0.046$ was taken from Ljungström et al. [59] and $S_{0(NH_3)} = 0.9$ from Bradley et al. [60], who measured sticking coefficient for ammonia on Pt(100).

Only two activation energies (E_{a24} and E_{a33}) were fitted in this subsystem, which has a total of 22 parameters. The 95% linearized confidence intervals for the fitted parameters are also given in Table 9. Table 10 summarizes the entropy changes for the reversible adsorption and desorption reactions and it can be seen that the values are between what is estimated for a completely localized specie and the estimated value for a 2D gas.

4.4. Parameters for NO_x regeneration

Table 11 summarizes the reaction rates and the kinetic parameters for the NO_x regeneration subsystem. The mechanism in this sub-model consists of summary reaction steps. Since it is difficult to know the reaction orders of these steps these were set to one in the model with respect to corresponding adsorbed specie. Reactions 34, 36 and 41 describe reactions between adsorbed species and gas phase CO_2. However, the reaction rate of these reactions does not contain the concentration of CO_2 since the model is not developed for varying CO_2 concentrations and the CO_2 concentration is constant in all experiments. The pre-exponential factor for reactions 39 and 40 are held constant at 10^{13} s^{-1}. In order to decrease the number of free parameters the pre-exponential factor and activation energy of reaction 37 are put to the same values as the parameters of reaction 34. This is also done for reaction 38, in which the parameters are put to the same value as the parameters in reaction 36.

Ten parameters out of 16 are fitted in the NO_x regeneration sub-model. The 95% linearized confidence interval for all these parameters are calculated and presented in Table 11. As can be seen in the table the confidence intervals of E_{a36}, E_{a41}, and A_{41} are large and with the experiments used in the simulations it is not possible to determine these parameters with high accuracy. However, the steps are necessary to regenerate the catalyst and describe the ammonia release properly.

Table 12
Number of sites

Site	Number of sites (mol/kg of washcoat)
Pt	2.7×10^{-2}
$BaCO_3$	$7.1 \times 10^{-2} \pm 0.14 \times 10^{-2}$
S_3	$10.1 \times 10^{-2} \pm 0.28 \times 10^{-2}$

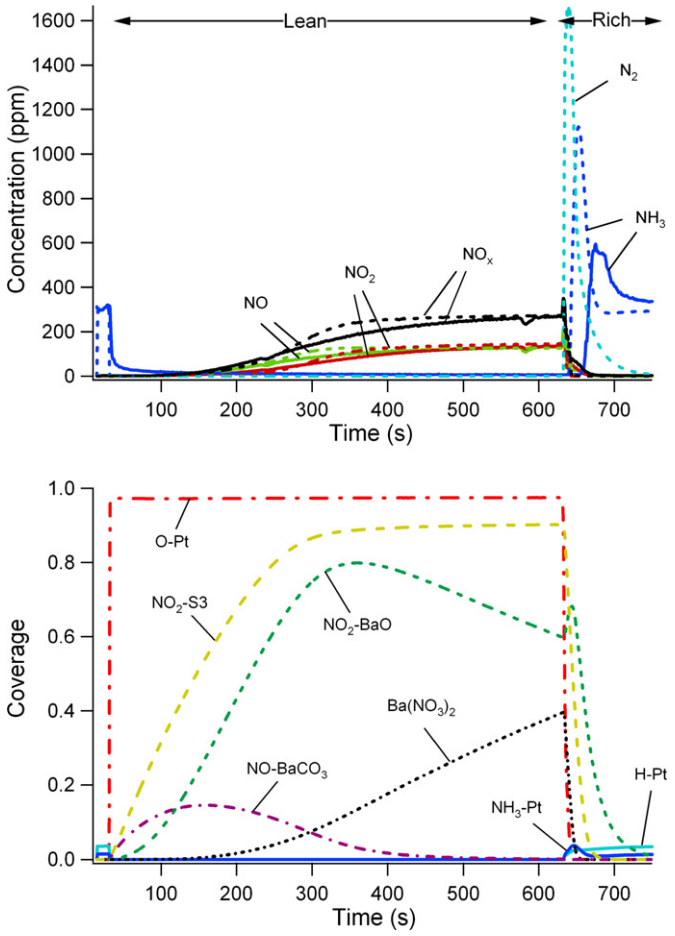

Fig. 1. Upper panel: Measured (solid) and calculated (dashed) outlet concentrations of NO, NO_2, N_2 and NH_3. The catalyst was exposed to 300 ppm NO, 8% O_2, 3% H_2O and 3% CO_2 during the lean period and to 300 ppm NO, 8000 ppm H_2, 3% H_2O and 3% CO_2 during the rich period at 300 °C. Lower panel: Calculated mean coverages.

4.5. Long NO_x storage and regeneration cycles

As mentioned above all four sub-models were used when modeling the transient experiments performed in this study. Figs. 1 and 2 show the experimental and simulated results from long NO_x storage and reduction cycles, i.e. cycles with a 600 s long lean period and a 300 s long rich period, conducted at 300 and 400 °C. The catalyst was exposed to 300 ppm NO, 8% O_2, 3% H_2O and 3% CO_2 during the lean period and to 300 ppm NO, 8000 ppm H_2, 3% H_2O and 3% CO_2 during the rich period. The upper panels in Figs. 1 and 2 show the NO, NO_2, NH_3 and N_2 concentrations and the lower panels the calculated mean coverages. A complete uptake of NO_x in the beginning of the lean period is observed in the

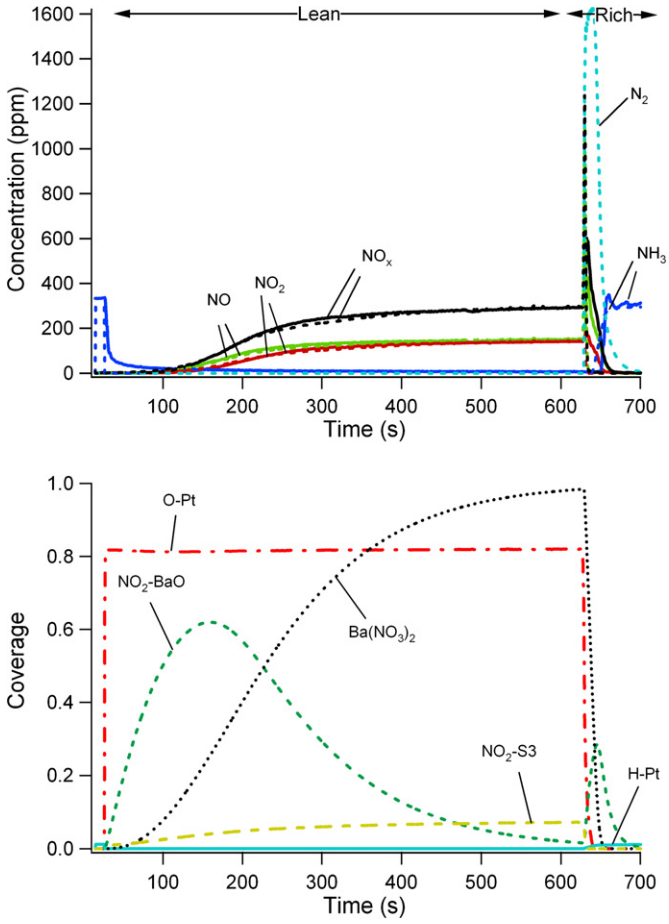

Fig. 2. Upper panel: Measured (solid) and calculated (dashed) outlet concentrations of NO, NO_2, N_2 and NH_3. The catalyst was exposed to 300 ppm NO, 8% O_2, 3% H_2O and 3% CO_2 during the lean period and to 300 ppm NO, 8000 ppm H_2, 3% H_2O and 3% CO_2 during the rich period at 400 °C. Lower panel: Calculated mean coverages.

experiments. The complete NO_x storage occurs for 70 s at both 300 and 400 °C as shown in Figs. 1 and 2. After 70 s of the lean period NO_x starts to break through but the storage is still substantial. Breakthrough of NO precedes the breakthrough of NO_2 and the NO concentration is higher than the NO_2 concentration at both temperatures during this period. The NO_x curve levels out after approximately 500 s at 300 °C and the NO and NO_2 concentrations are approaching steady state. However, a significant NO_x uptake is still observed. The steady state levels of NO and NO_2 are reached around 400 s in the experiment conducted at 400 °C.

The NO oxidation capacity of the catalyst is important for the storage behavior. It is kinetically limited at low temperatures and thermodynamically limited at higher temperatures [49]. According to thermodynamic equilibrium levels the NO and NO_2 concentrations should be equal at 400 °C, when using 8% O_2 [49], which is observed in the end of the lean period in Fig. 2. At temperatures below 400 °C the NO_2 concentration should be higher than the NO concentration according to the thermodynamics, which is observed at 300 °C over Pt supported on silica [32] and alumina [49]. In Fig. 1 it can be seen that the NO oxidation capacity for this catalyst is low at 300 °C. Only 135 ppm NO_2 is produced from 300 ppm NO and 8% O_2 after 600 s, which is close to 50% of the outlet NO_x concentration. The reason for this is that the addition of barium decreases the oxidation capacity of platinum [61]. The steady state NO and NO_2 concentrations predicted by the model is in accordance with the experiments. Furthermore, the model can describe the complete uptake of NO_x in the beginning of the lean period, the NO_x breakthrough, and the slow NO_x storage in the end of the lean period very well at both 300 °C and 400 °C.

The simulations predict high oxygen coverage over Pt during the lean periods at both 300 °C and 400 °C as shown in the plots of the calculated mean coverages in Figs. 1 and 2. A lower oxygen coverage is predicted at the higher temperature, which is due to an increase in the desorption rate of oxygen at 400 °C. Furthermore, the calculations of the coverages presented in Fig. 1 show that NO_x is initially stored as NO over $BaCO_3$ and as NO_2 over S_3 at 300 °C. The storage of NO over $BaCO_3$ is only observed in the beginning of the lean period at this temperature. When the more stable nitrates are formed on the surface the adsorption of the loosely bound NO species is hindered, thus resulting in a decrease in coverage of this specie. As mentioned earlier, investigations have shown that NO can be stored directly over Pt/Ba/Al catalysts without being oxidized into NO_2 first [10,31].

The NO_2–S_3 is formed via two routes at 300 °C: NO_2 is either produced via NO oxidation over Pt, which is followed by adsorption over S_3 or NO is adsorbed on S_3 which is then further oxidized by O–Pt into NO_2–S_3. A stationary level of the NO_2–S_3 coverage is predicted at the end of the lean period. No NO_2–$BaCO_3$ is observed in the calculations, which means that the formation of BaO–NO_2 (reaction 11) is very fast. Barium nitrate ($Ba(NO_3)_2$) is formed when the coverage of BaO–NO_2 is high enough. According to the calculations, NO_x is stored as NO_2 via the disproportionation reaction and over S_3 at 300 °C. In addition, NO is stored directly on $BaCO_3$ at this temperature.

The calculations of the coverages presented in Fig. 2 show that BaO–NO_2 is the first surface specie that is formed over the storage components at 400 °C. When the lean period proceeds BaO–NO_2 goes through a maximum and barium nitrate builds up on the surface, which was also the case at 300 °C. In a DRIFT study of NO adsorption in the presence of O_2 at 350 °C performed by Nova et al. [11], the intensities of the IR spectra were plotted versus time and a similar pattern of the progression of the surface species was observed. In the calculations performed here all active $BaCO_3$ sites are converted into $Ba(NO_3)_2$ at the end of the lean phase. This is also in agreement with in situ FTIR experiments performed by Nova et al. [10], who found that nitrates are the most abundant adsorbed specie at catalyst saturation. In addition, a small amount of NO_x is stored at the second storage site as NO_2–S_3 at 400 °C. At this temperature NO_2–S_3 is formed only via the first route described above, i.e. NO is oxidized to NO_2 over Pt and the NO_2 produced is stored on S_3. According to the calculations most of the NO_x is stored via the disproportionation route and very little is stored on S_3 at this high temperature.

The NO_x adsorbed is released from the storage sites when switching from lean to rich conditions, due to reactions between the stored NO_x and hydrogen on platinum to produce gas phase NO. This can be observed in Figs. 1 and 2 as an increase in the NO and NO_x concentration immediately after the switch from lean to rich. It can also be seen that the amount of released NO_x into the gas phase is larger at 400 °C than at 300 °C. The increase in the NO concentration, the steady state level of NO_x in the rich period (0 ppm), and the temperature dependence of the released NO_x in the gas phase is described well by the model.

According to the model N_2 is formed almost immediately after the lean/rich switch, before ammonia is detected, at both temperatures. The N_2 concentration reaches a maximum concentration of 1550 ppm at 300 °C and 1600 ppm at 400 °C. After the maximum peak the concentration slowly decreases and reaches zero when the rich period is complete. The N_2 concentration was not measured in the experiments performed in this study. However, other investigations of NO_x reduction with hydrogen have shown that N_2 is detected directly when introducing H_2 to the catalyst, before the ammonia evolution [24,29,62]. In Figs. 1 and 2 it can be seen that

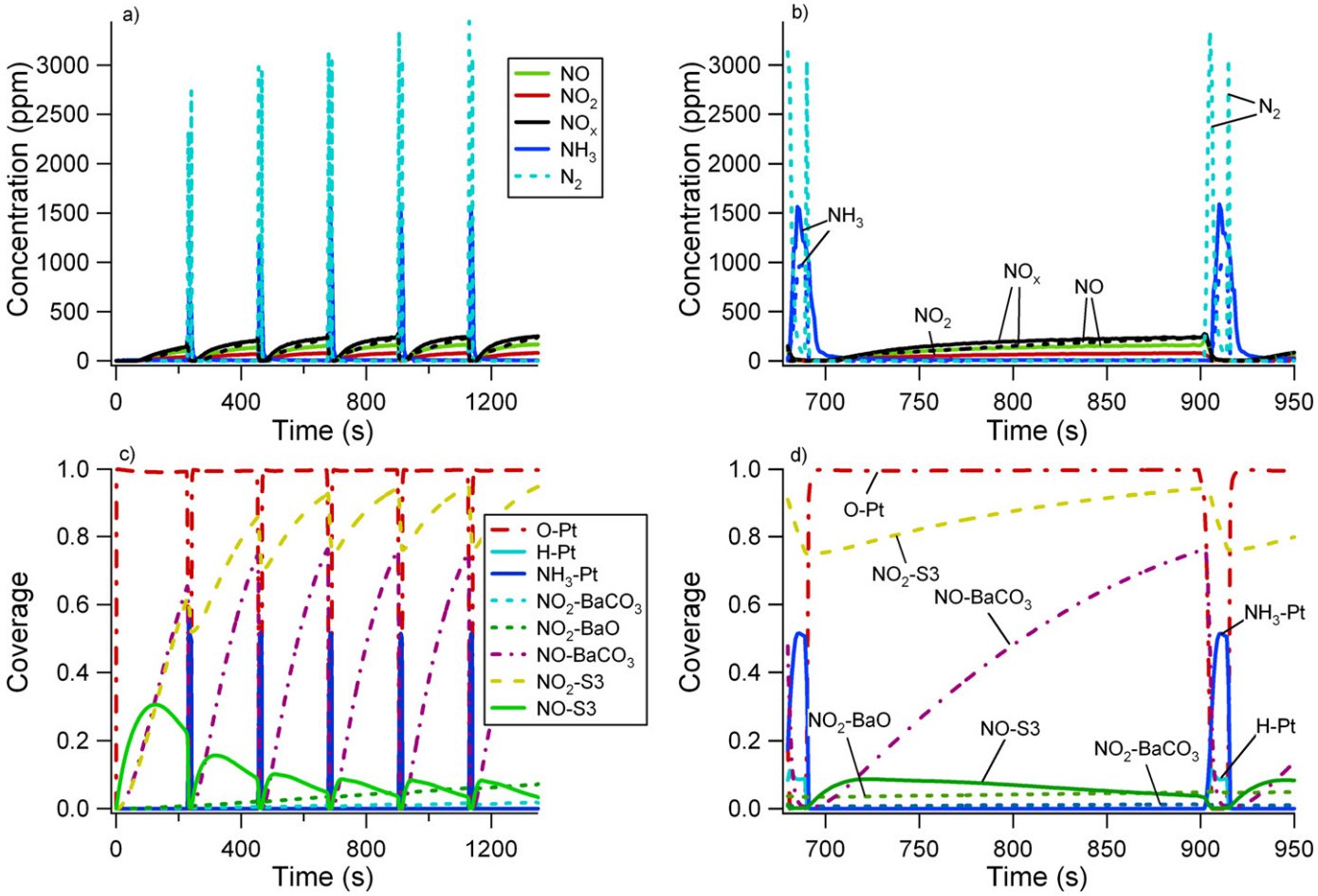

Fig. 3. Upper panels: Measured (solid) and calculated (dashed) outlet concentrations of NO, NO_2, N_2 and NH_3. The catalyst was exposed to 300 ppm NO, 8% O_2, 3% H_2O and 3% CO_2 during the lean periods (210 s) and to 300 ppm NO, 16 000 ppm H_2, 3% H_2O and 3% CO_2 during the rich periods (15 s) at 200 °C. Lower panel: Calculated mean coverages. A magnification of one lean and rich period is shown to the right.

the ammonia concentration is observed approximately 25 s after the introduction of the reducing agent. At both 300 and 400 °C the ammonia concentration raises to above the inlet NO_x concentration; this is followed by a decrease in the concentration, which finally approaches a stationary level. The model predicts a higher ammonia concentration at 300 °C compared to 400 °C, which also is observed experimentally. However, the maximum ammonia peak is overestimated in the simulation and the delay in the NH_3 signal is shorter than in the experiment at 300 °C. The NH_3 concentration at 400 °C is well described in the simulations, both the stationary level and time delay.

4.6. Lean/rich cycling

Shorter lean and rich periods were conducted at 200, 300 and 400 °C, in order to verify the model on experiments closer to real applications. The catalyst was exposed to 300 ppm NO, 8% O_2, 3% H_2O and 3% CO_2 during the 210 s long lean periods. After each lean phase the catalyst was regenerated for 15 s by exposing it to 300 ppm NO, 16 000 ppm H_2, 3% H_2O and 3% CO_2. The results from the experiments and the simulations are presented in Figs. 3–5. The upper panels show the NO, NO_2, NH_3 and N_2 concentrations and the lower panels the calculated mean coverages. In the figures it can be seen that the cyclic steady state is reached in the third or fourth cycle of the experiments and a gradual decrease in the storage capacity is observed in the earlier cycles. The catalyst was completely regenerated before starting the first cycle and as seen in the figures a 15 s long rich period is not enough to regenerate the catalyst entirely.

Fig. 3 shows the results from 200 °C. The storage capacity is substantial even at this low temperature. It takes about 60 s before NO_x breaks through in the first cycle; the complete uptake is then reduced to approximately 10 s in the following cycles. The experiment also shows that the NO oxidation capacity is low at 200 °C. In addition, it can be seen that the maximum concentration of ammonia in the rich periods increases when the cycling proceeds. It reaches cyclic steady state in the fourth cycle.

In order to describe the substantial NO_x storage and the low NO oxidation capacity at this temperature it was crucial to add NO adsorption to the model. The simulated total NO_x concentration fits well with the experiment and the model can predict the gradual decrease in the storage capacity occurring during cycling. As in the simulations presented above high oxygen coverage over Pt is also calculated at 200 °C in the lean periods. When switching to rich conditions the oxygen coverage decreases to zero. In contrast to the storage occurring at 400 °C, the plot of the coverages calculated at 200 °C reveals that NO_x is stored on S_3 to a large extent.

According to the calculations NO is first adsorbed on S_3, which is then oxidized into NO_2–S_3. The coverage of NO–S_3 is the highest in the first cycle and decreases when the cycling proceeds. This surface specie is easily reduced and the coverage is zero in the beginning of each lean period. The coverage of NO_2–S_3 on the other hand is not completely reduced during the rich periods which results in an accumulation of this surface specie until cyclic steady

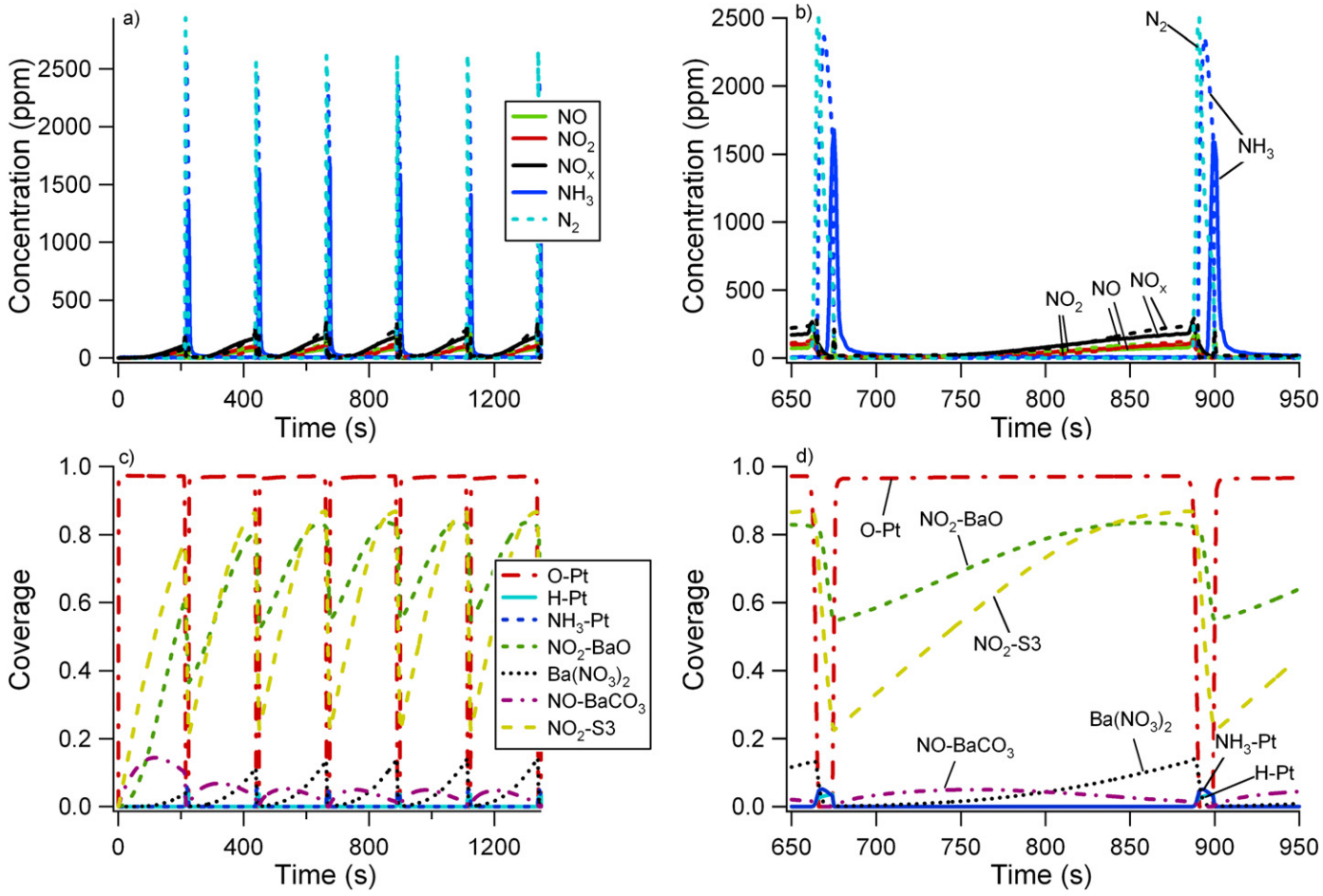

Fig. 4. Upper panels: Measured (solid) and calculated (dashed) outlet concentrations of NO, NO_2, N_2 and NH_3. The catalyst was exposed to 300 ppm NO, 8% O_2, 3% H_2O and 3% CO_2 during the lean periods (210 s) and to 300 ppm NO, 16 000 ppm H_2, 3% H_2O and 3% CO_2 during the rich periods (15 s) at 300 °C. Lower panel: Calculated mean coverages. A magnification of one lean and rich period is shown to the right.

state is reached. The $BaCO_3$ sites are also utilized at 200 °C. Most of the sites are used for NO adsorption, which are easily reduced, but a low amount of the $BaCO_3$ sites are also converted into BaO–NO_2. The BaO–NO_2 sites are very difficult to reduce at this low temperature and the coverage is therefore increasing steadily as the experiment continues.

Additionally, the simulated NH_3 concentration during the rich events fits well with experimental observations. According to the model nitrogen is formed before ammonia is observed and it has a maximum concentration of about 3000 ppm. This is in agreement with experimental findings, where Nova et al. [24] observed nitrogen formation before NH_3. Moreover, two nitrogen peaks appear in the simulations, when switching from lean to rich conditions and when switching back from rich to lean conditions. The reason for the second nitrogen peak, occurring when starting the lean period, is that the hydrogen on platinum and ammonia on platinum, from the rich period, react with the incoming NO_x to form N_2 when starting the lean period. Since no hydrogen is present in the gas phase during the lean period, the reaction between incoming NO_x and the reduced species on platinum from the rich period produce nitrogen rather than ammonia. The ammonia coverage over Pt is calculated to be in the order of 0.5 and the hydrogen coverage is approximately 0.1 at this temperature. This is consistent with experimental findings by Lietti et al. [41]. They observed two nitrogen peaks both when starting the rich period and when shutting of the hydrogen at 200 °C. They explained the latter N_2 peak by small residues of oxygen in the feed gas that reacts with adsorbed hydrogen on platinum.

The results from the cycling experiments and simulations conducted at 300 and 400 °C are presented in Figs. 4 and 5. All NO_x in the first cycle of both experiments is adsorbed for approximately 70 s, which is the same time as for the complete uptake in the long lean periods conducted at the same temperatures (see Figs. 1 and 2). The time for complete uptake is reduced in the following cycles to 45 s at 300 °C and to 55 s at 400 °C, which shows that the reduction is more efficient at higher temperatures. As can be seen in Fig. 4 the NO_x curve and the NO and NO_2 concentrations during the lean periods are well described by the model at 300 °C. The model is also able to describe the decrease in the storage capacity when the cycling progresses. As mentioned earlier, the oxidation of nitrites into nitrates over S_3 (reaction 19) was crucial in order to describe the storage capacity at 300 °C. As can be seen in Fig. 4 the storage over the second storage site (S_3) is significant also at this temperature. However, in contrast to the simulation of the cycling experiment conducted at 200 °C NO_x is stored over $BaCO_3$ to a larger extent. A coverage of $Ba(NO_3)_2$ is predicted in the lean periods.

Moreover, the regeneration of NO_2–S_3 and BaO–NO_2 is more efficient at 300 °C than at 200 °C. Nevertheless, the species are not completely reduced which results in accumulation of the surface species. A consequence of the increase in the coverage of BaO–NO_2 is that more $Ba(NO_3)_2$ is formed, which is also not completely reduced in the rich periods when it reaches a certain level. Also at this temperature, the model predicts N_2 to appear immediately when switching to rich conditions. However, only one nitrogen peak is calculated at this temperature. The nitrogen peak observed

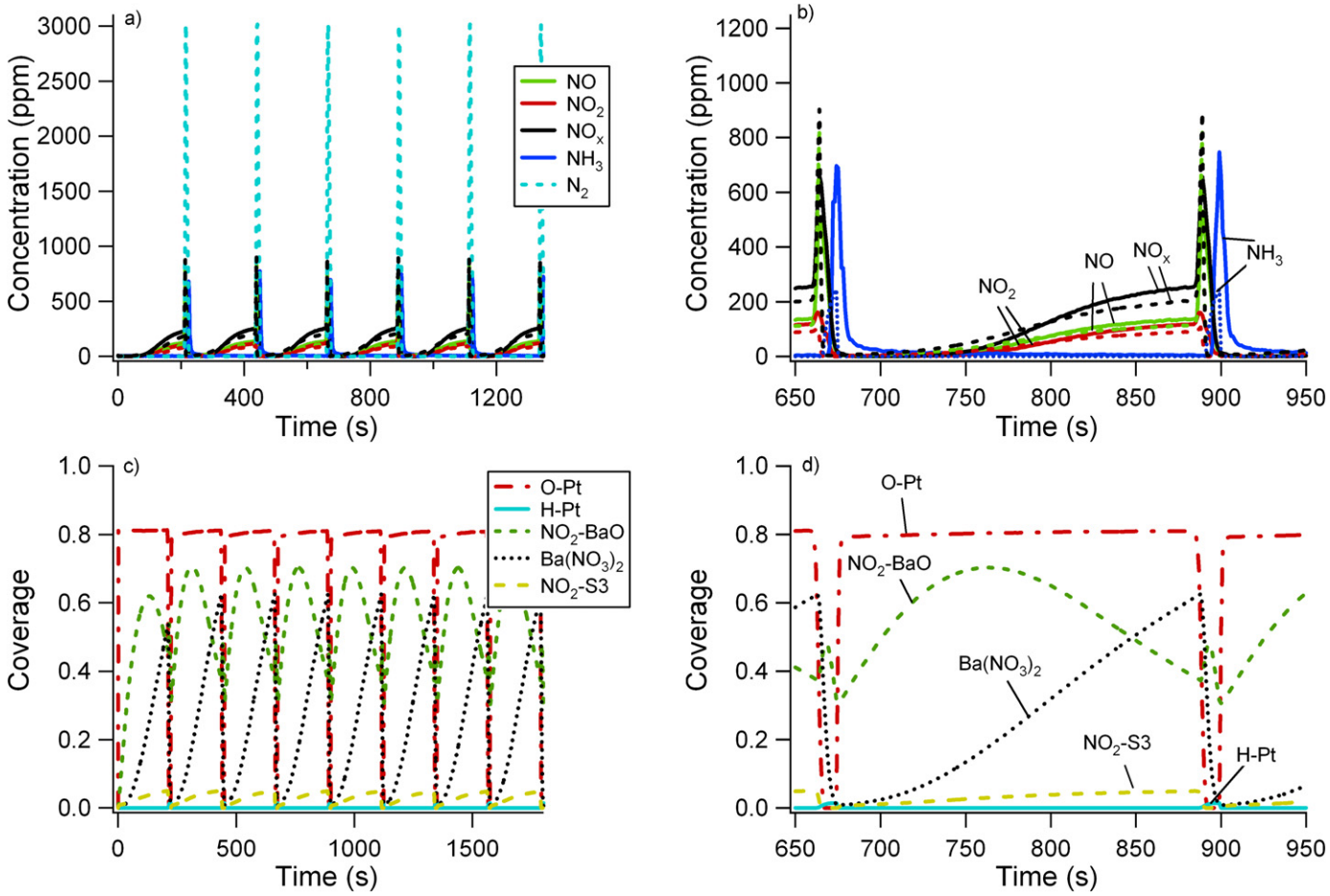

Fig. 5. Upper panels: Measured (solid) and calculated (dashed) outlet concentrations of NO, NO_2, N_2 and NH_3. The catalyst was exposed to 300 ppm NO, 8% O_2, 3% H_2O and 3% CO_2 during the lean periods (210 s) and to 300 ppm NO, 16 000 ppm H_2, 3% H_2O and 3% CO_2 during the rich periods (15 s) at 400 °C. Lower panel: Calculated mean coverages. A magnification of one lean and rich period is shown to the right.

in the simulations at 200 °C when starting the lean period is not seen in the simulations at 300 °C. This is consistent with experimental observations by Lietti et al. [41], who found a second N_2 peak at lower temperatures (200 °C), but not at 300 and 400 °C. The coverage of ammonia and hydrogen on platinum from the rich period is much lower at this temperature and thus there is no nitrogen formed when starting the lean period. The NH_3 concentration predicted in the simulations are higher than the experiments, as can be seen in Fig. 4. However, the shape of the ammonia peak agrees well with the experiment and it is only 4 s difference in time when the peak occurs between the model and the experiment.

The results from the lean/rich cycling presented in Fig. 5 shows that the NO oxidation is approaching the thermodynamic level at 400 °C, which is well described by the model. In the lower panel of Fig. 5 the calculated mean coverages are shown and it can be seen that most of the $BaCO_3$ sites are converted into $Ba(NO_3)_2$. However, a 240 s long lean period is not long enough to transform all $BaCO_3$ sites into $Ba(NO_3)_2$. The coverage of BaO–NO_2 is still significant when switching to rich conditions, which results in an incomplete reduction of this specie during the short rich period. BaO–NO_2 is accumulated on the surface after the rich period and as a consequence more $Ba(NO_3)_2$ can be formed in the following lean period. Moreover, the model predicts a low amount of NO_2–S_3 during the lean periods. This specie is adsorbed in the same manner as in the long lean period conducted at 400 °C and it is also completely reduced during the rich periods.

From the results presented above it is clear that the second storage site (S_3) is important in order to explain NO_x storage at low temperatures and the disproportionation reaction is essential to describe the storage at high temperatures. The experimental results show that the amount of ammonia formed during the rich period is lower at 400 °C compared to 200 and 300 °C. This trend is described by the model, but the ammonia formation is lower in the model. Moreover, the model predicts a delay in the NH_3 signal, which is only 3 s shorter than the ammonia delay observed in the experiment. The maximum nitrogen concentration is predicted by the model to 3000 ppm and only one N_2 peak appears at this temperature, due to the low coverage of ammonia and hydrogen in the rich period. This was also found experimentally by Lietti et al. [41].

4.7. Validation of the model

The model was validated by simulating experiments that were not included in the fitting procedure. The validation experiments were alternating lean and rich periods conducted at 200, 300 and 400 °C. The lean periods were 60 s long and the feed contained 300 ppm NO, 8% O_2, 3% H_2O and 3% CO_2. In the rich periods the catalyst was exposed to 300 ppm NO, 16 000 ppm H_2, 3% H_2O and 3% CO_2 for 15 s. Figs. 6–8 show the experimental and simulated results from the validation experiments at 200, 300 and 400 °C. The upper panels in the figures show the NO, NO_2, NH_3, and N_2 concentrations and the lower panels show the calculated mean coverages. Due to the shorter lean period in the validation

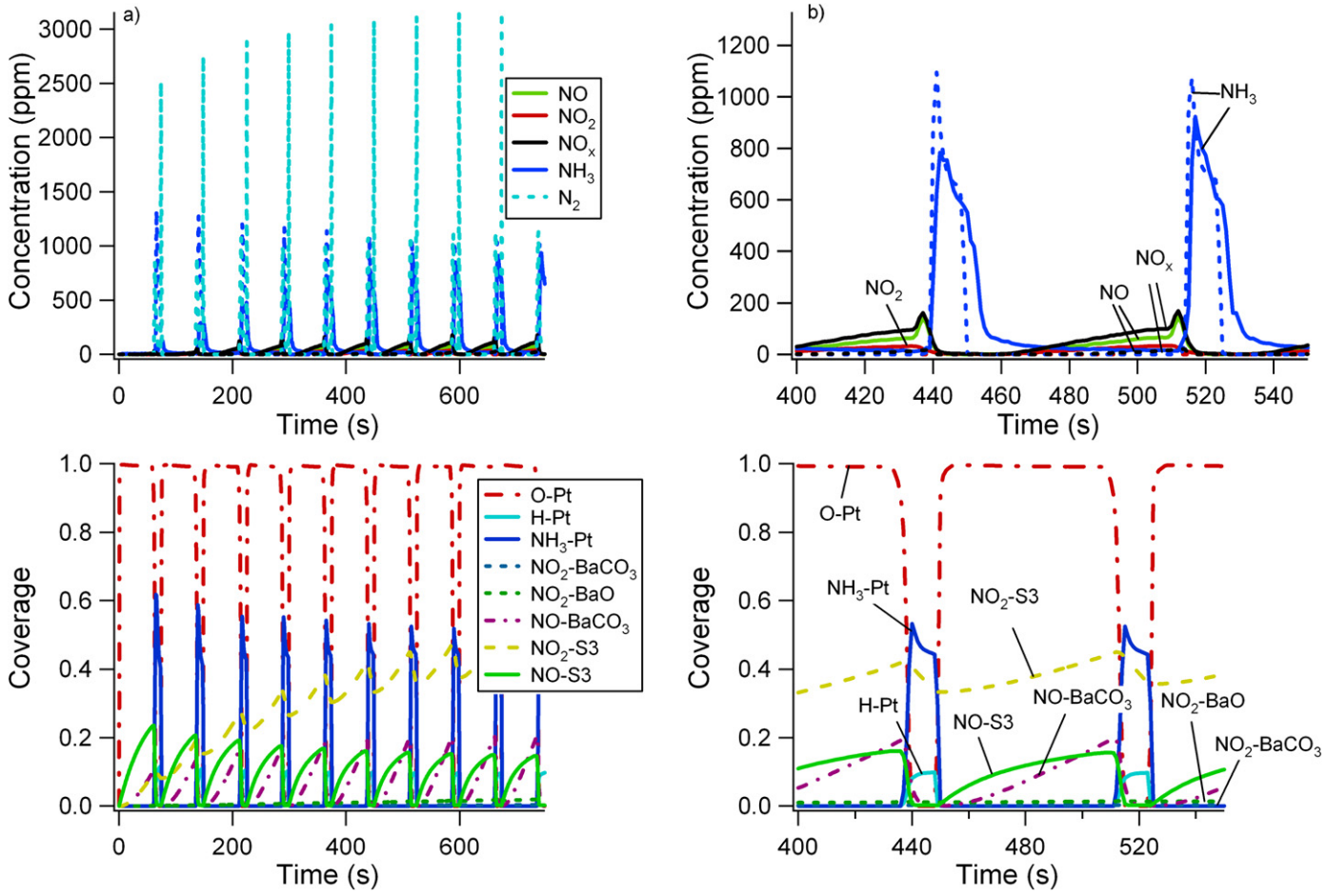

Fig. 6. Upper panels: Measured (solid) and calculated (dashed) outlet concentrations of NO, NO_2, N_2 and NH_3 from the model validation. The catalyst was exposed to 300 ppm NO, 8% O_2, 3% H_2O and 3% CO_2 during the lean periods (60 s) and to 300 ppm NO, 16 000 ppm H_2, 3% H_2O and 3% CO_2 during the rich periods (15 s) at 200 °C. Lower panel: Calculated mean coverages. A magnification of one lean and rich period without the N_2 concentration is shown to the right.

experiments the amount of NO_x adsorbed is lower than in the experiments used in the fitting procedure, which will effect the regeneration of the catalyst.

As can be seen in the figures all NO_x that enters the catalyst is adsorbed completely during the lean periods at 300 and 400 °C. This is well predicted by the model. At 200 °C there is a complete capture in the first two cycles. However, when the cycling proceeds NO_x starts to break through and in the last cycles the concentration of NO_x reaches 100 ppm at the end of the lean period. The model predicts no NO_x breakthrough during the lean periods for all cycles also at 200 °C. When switching to rich conditions the NO_x release peak appears at all temperatures. The peak is low at 200 and 300 °C; at 200 °C the NO_x concentration increases to around 170 ppm from 100 ppm in the last cycles and to 40 ppm from 0 ppm at 300 °C. The peaks predicted by the model are also low at these temperatures. The NO_x release peaks reach above 200 ppm, from 0 ppm during the lean periods, in the last cycles at 400 °C. This raise in NO_x concentration is also well predicted by the model.

According to the simulations, nitrogen is formed immediately when switching to rich conditions, before the NH_3 evolution, at all temperatures. The nitrogen peak increases with the cycles and reaches the highest concentration at 200 °C (around 3000 ppm). In addition, two N_2 peaks appear during rich conditions at 200 °C; the first one when switching to rich conditions and the second when switching back to lean conditions. This was also the case for the 210 s/15 s cycles which is explained above and it is in agreement with experimental findings [41]. The NH_3 peak predicted by the model at 200 °C fits very well with experimental data. At 300 °C the ammonia concentration is somewhat overrated by the model; however, the timing of the ammonia evolution is well predicted. At the highest simulated temperature the ammonia concentration is underestimated, but the evolution of NH_3 is predicted only about 3 s earlier than in the experiments. The predicted coverages are similar to the simulations of the foregoing longer cycles. However, the coverages never reach the same levels since the lean periods are shorter.

5. Conclusions

A detailed kinetic model that describes NO_x storage and reduction over Pt/Ba/Al with hydrogen as the reducing agent was developed in this work. The model was developed to explain experiments in the presence of H_2O and CO_2. Four sub-models constitute the model: (i) NO oxidation over Pt, (ii) NO_x storage, (iii) NO_x reduction over Pt, and (iv) NO_x regeneration. The model is based on earlier developed models for NO oxidation, NO_x storage and NO_x reduction with hydrogen. The kinetic parameters are derived from kinetic gas theory, transition state theory, statistical thermodynamics, thermodynamic constraints, the literature, experiments, or fitted in this work using the least square method. The fitted parameters are given with the 95% linearized confidence intervals.

Due to the presence of CO_2 in the gas feed the barium sites in the model are in the carbonate form according to a recent exper-

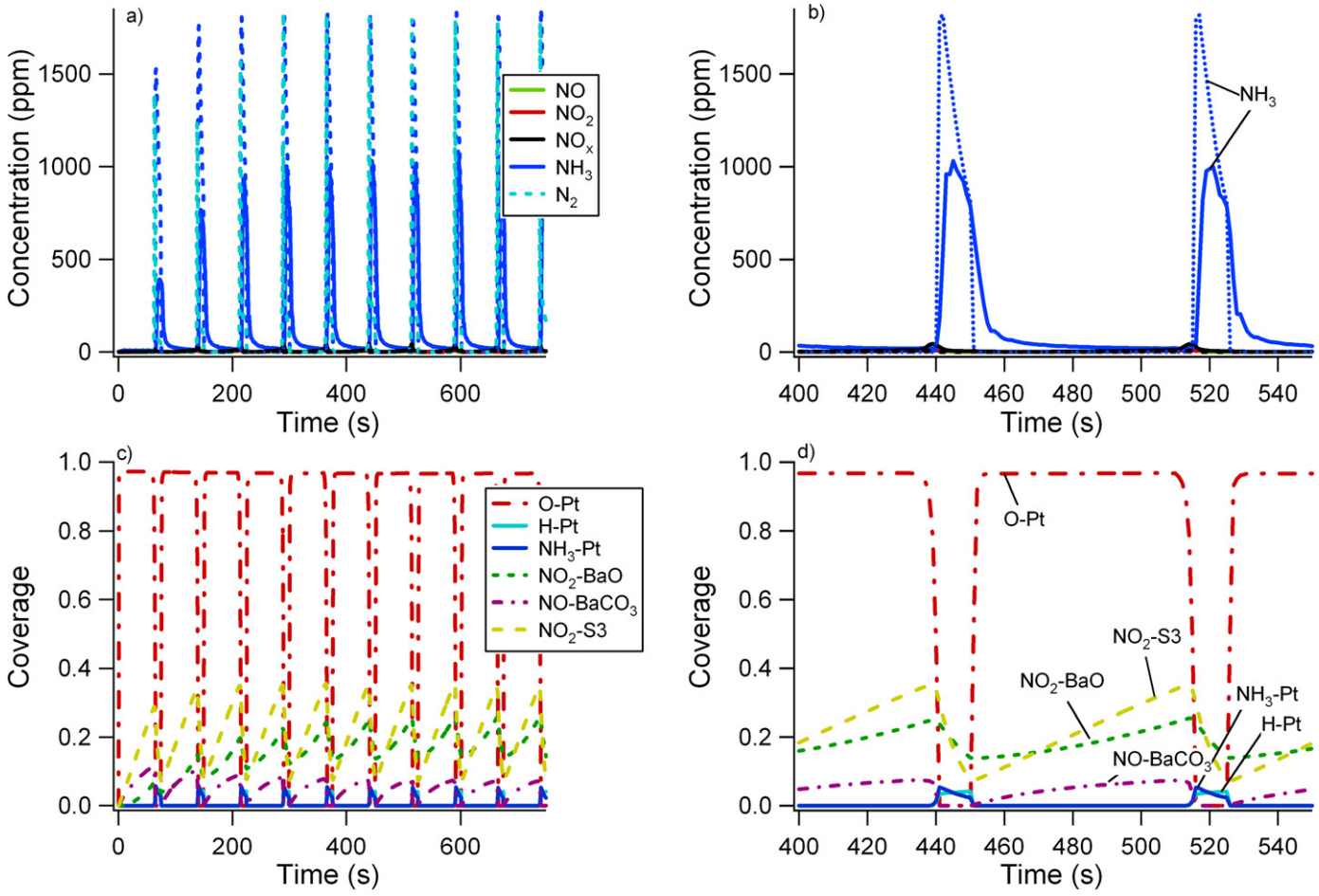

Fig. 7. Upper panels: Measured (solid) and calculated (dashed) outlet concentrations of NO, NO_2, N_2 and NH_3 from the model validation. The catalyst was exposed to 300 ppm NO, 8% O_2, 3% H_2O and 3% CO_2 during the lean periods (60 s) and to 300 ppm NO, 16 000 ppm H_2, 3% H_2O and 3% CO_2 during the rich periods (15 s) at 300 °C. Lower panel: Calculated mean coverages. A magnification of one lean and rich period without the N_2 concentration is shown to the right.

imental investigation. A second storage site denoted S_3 is also introduced in the model. Multiple storage sites have been suggested several times in the literature based on experimental findings, but the physical explanation differs. It is suggested to be storage on (i) alumina and barium, (ii) surface and bulk barium, (iii) barium sites close and far from the noble metal, etc. Both NO and NO_2 can be stored over $BaCO_3$ and S_3. The storage of NO_2 over $BaCO_3$ takes place via the disproportionation route. Nitrogen oxide adsorbed over S_3 can be further oxidized to NO_2 by reacting with oxygen on neighboring Pt sites. Hence, there are two possible routes for NO oxidation in the proposed model. The model can describe the complete uptake of NO_x in the beginning of the lean period, the NO_x breakthrough, and the slow NO_x storage in the end of the lean period experimentally observed. According to the model NO_x adsorption on $BaCO_3$ becomes more significant at higher temperatures; most of the NO_x is stored via the disproportionation route and very little is stored on S_3. The second storage site (S_3) is important for the low temperature storage; the disproportionation reaction does not occur at the lowest temperature simulated. Furthermore, the model can predict the gradual decrease in the storage capacity observed before reaching cyclic steady state in the lean/rich cycling experiments.

The regeneration period is also well described by the model. In the proposed model hydrogen cleans the Pt surface from adsorbed oxygen to facilitate NO dissociation, N_2 formation, and NH_3 formation. In addition, the reducing agent reacts directly with species adsorbed on the storage sites. The model predicts N_2 formation immediately after the lean/rich switch, before ammonia is detected. By introducing reactions according to SCR chemistry between adsorbed surface species and the NH_3 formed under the rich period, the delay in the NH_3 signal observed in the experiments could be described by the model. In addition, the model predicts the regeneration to be more efficient at higher temperatures than at lower temperatures.

Experiments that were not included in the development of the model were conducted to validate the model and a good agreement was found between the validation experiments and the model. In these experiments the catalyst was exposed to 300 ppm NO, 8% O_2, 3% H_2O and 3% CO_2 for 60 s and the rich period consisted of 300 ppm NO, 16 000 ppm H_2, 3% H_2O and 3% CO_2 for 15 s. The experiment was repeated at three temperatures, 200, 300 and 400 °C. At 300 and 400 °C no NO_x breaks through in the lean period and this is well described by the model. The model also predicts no NO_x in the lean period at 200 °C, but experimentally NO_x is observed after two cycles. Generally the ammonia peaks in the rich periods are well described by the model. At 300 °C the peak is somewhat to high and at 400 °C somewhat to low. Further, at 200 °C the agreement between the ammonia production predicted by the model and the experiment is very good. The timing of the ammonia peak is only 3 s earlier in the model than in the experiment at 400 °C. At both 200 and 300 °C the timing of the ammonia evolution is very well predicted by the model.

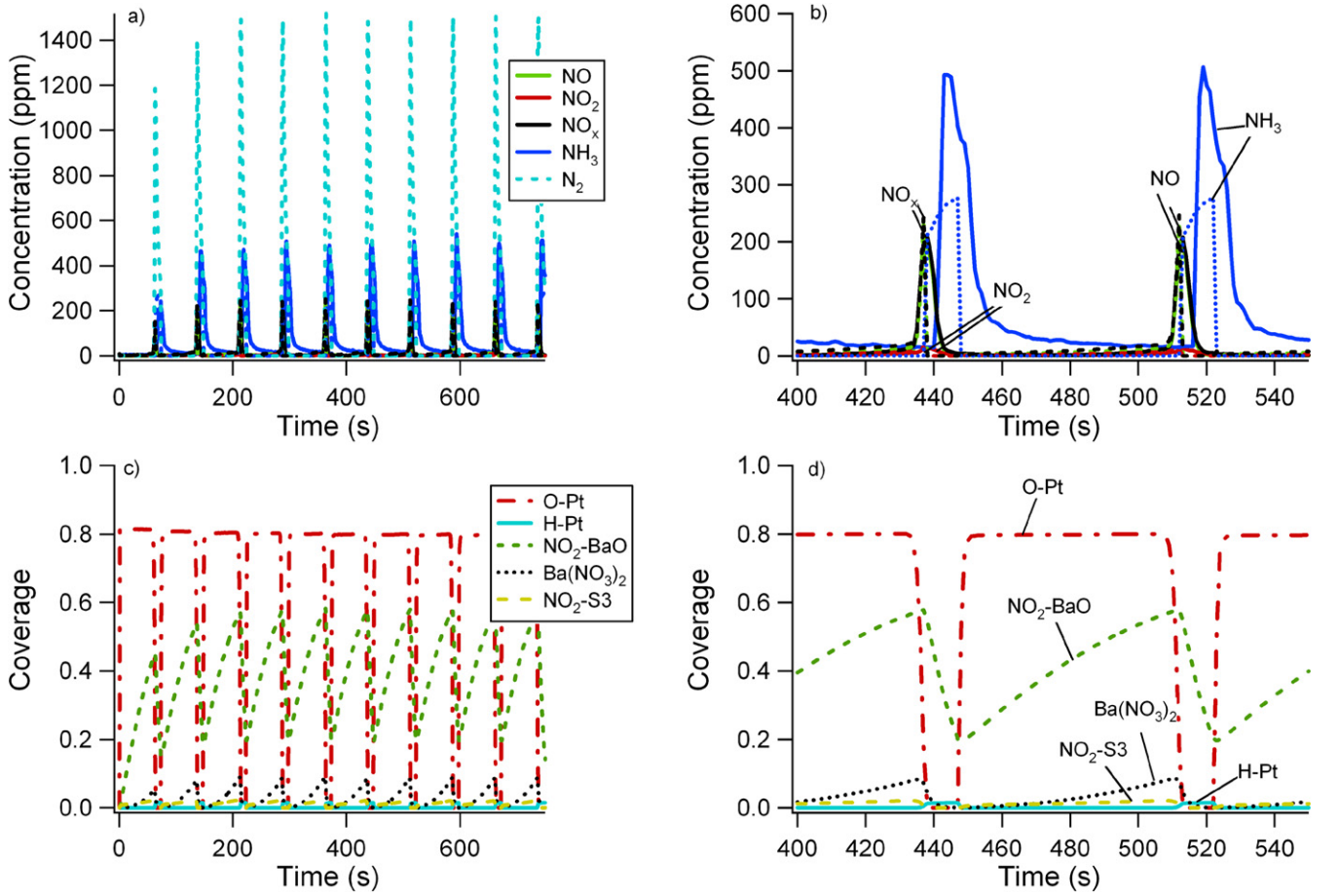

Fig. 8. Upper panels: Measured (solid) and calculated (dashed) outlet concentrations of NO, NO_2, N_2 and NH_3 from the model validation. The catalyst was exposed to 300 ppm NO, 8% O_2, 3% H_2O and 3% CO_2 during the lean periods (60 s) and to 300 ppm NO, 16 000 ppm H_2, 3% H_2O and 3% CO_2 during the rich periods (15 s) at 400 °C. Lower panel: Calculated mean coverages. A magnification of one lean and rich period without the N_2 concentration is shown to the right.

Acknowledgments

This work was carried out at the Competence Centre for Catalysis, Chalmers University of Technology and at Cummins Inc. Cummins Inc. is gratefully acknowledged for the financial support. One author (Louise Olsson) would also like to acknowledge the Swedish Research Council (Contract: 621-2003-4149 and 621-2006-3706) for additional support.

Appendix A. Nomenclature

A	area of a Pt site (m^2/site)
A_{ads}	pre-exponential factor for adsorption ($m^3/(s\,kg_{wc})$)
A_j	pre-exponential factor for reaction j [$m^3/(s\,kg_{wc})$[1] or $mol/(s\,kg_{wc})$[2]]
A_k	wall area in tank k (m^2)
$c_{g,i,k}$	concentration of component i in tank k in the gas bulk (mol/m^3)
$c_{s,i,k}$	concentration of component i in tank k at the catalyst surface (mol/m^3)
D	diffusion coefficient (m^2/s)
D_{ref}	diffusion coefficient at temperature T_{ref} (m^2/s)
d	channel width (m)
$E_{a,j}$	activation energy of reaction j (J/mol)
$F_{i,k-1}$	molar flow of component i into tank k (mol/s)
$F_{i,k}$	molar flow of component i out of tank k (mol/s)
h	Planck's constant (J s)
K_{eq}	equilibrium constant (–)
k_B	Boltzmann's constant (J/K)
$k_{c,i,k}$	mass transfer coefficient of component i in tank k (m/s)
k_j	rate constant of reaction j [$m^3/(s\,kg_{wc})$[1] or $mol/(s\,kg_{wc})$[2]]
M	molar mass (kg/mol)
$m_{wc,k}$	mass of washcoat (active catalyst) in tank k (kg_{wc})
N_A	Avogadros' number (mol^{-1})
N_{cat}	number of active sites per kg catalyst (mol/kg_{wc})
R	molar gas constant (J/(mol K))
$r_{j,k}$	rate of reaction j in tank k ($mol/(s\,kg_{wc})$)
Re	Reynolds number (–)
$S(0)$	sticking coefficient for zero coverage (–)
Sc	Schmidt number (–)
Sh	Sherwood number (–)
Sh_∞	asymptotic Sherwood number (–)
T	temperature (K)
T_{ref}	reference temperature (673 K) used in the simulations (K)
z	distance from the entrance of the monolith channel (m)
z_m	dimensionless axial distance for the mass transfer (–)
$\theta_{i,k}$	mean coverage of surface species i in tank k (–)
v	flow speed (m/s)
$\upsilon_{i,j}$	stoichiometric coefficient for component i in reaction j (–)

[1] For adsorption.
[2] For desorption and reaction.

References

[1] N. Takahashi, H. Shinjoh, T. Iijima, T. Suzuki, K. Yamazaki, K. Yokota, H. Suzuki, N. Miyoshi, S. Matsumoto, T. Tanizawa, T. Tanaka, S. Tateishi, K. Kasahara, Catal. Today 27 (1996) 63–69.
[2] W.S. Epling, A. Yezerets, N.W. Currier, Appl. Catal. B Environ. 74 (2007) 117–129.
[3] S. Salasc, M. Skoglundh, E. Fridell, Appl. Catal. B Environ. 36 (2002) 145–160.
[4] S. Erkfeldt, E. Jobson, M. Larsson, Top. Catal. 16 (2001) 127–131.
[5] E. Fridell, H. Persson, B. Westerberg, L. Olsson, M. Skoglundh, Catal. Lett. 66 (2000) 71–74.
[6] E. Fridell, M. Skoglundh, B. Westerberg, S. Johansson, G. Smedler, J. Catal. 183 (1999) 196–209.
[7] L. Olsson, H. Persson, E. Fridell, M. Skoglundh, B. Andersson, J. Phys. Chem. B 105 (2001) 6895–6906.
[8] L. Olsson, E. Fridell, M. Skoglundh, B. Andersson, Catal. Today 73 (2002) 263–270.
[9] T. Kobayashi, T. Yamada, K. Kayano, SAE Tech. Pap. Ser. 97-07-45 (1997).
[10] I. Nova, L. Castoldi, L. Lietti, E. Tronconi, P. Forzatti, F. Prinetto, G. Ghiotti, J. Catal. 222 (2004) 377–388.
[11] I. Nova, L. Castoldi, F. Prinetto, V. Dal Santo, L. Lietti, E. Tronconi, P. Forzatti, G. Ghiotti, R. Psaro, S. Recchia, Top. Catal. 30–31 (2004) 181–186.
[12] L. Castoldi, I. Nova, L. Lietti, P. Forzatti, Catal. Today 96 (2004) 43–52.
[13] H. Mahzoul, J.F. Brilhac, P. Gilot, Appl. Catal. B Environ. 20 (1999) 47–55.
[14] W.S. Epling, J.E. Parks, G.C. Campbell, A. Yezerets, N.W. Currier, L.E. Campbell, Catal. Today 96 (2004) 21–30.
[15] U. Elizundia, R. Lopez-Fonseca, I. Landa, M.A. Gutierrez-Ortiz, J.R. Gonzalez-Velasco, Top. Catal. 42–43 (1–4) (2007) 37–41.
[16] M. Piacentini, M. Maciejewski, A. Baiker, Appl. Catal. B Environ. 60 (2005) 265–275.
[17] S. Poulston, R.R. Rajaram, Catal. Today 81 (2003) 603–610.
[18] Z. Liu, J.A. Anderson, J. Catal. 224 (2004) 18–27.
[19] P. Jozsa, E. Jobson, M. Larsson, Top. Catal. 30–31 (2004) 177–180.
[20] D. James, E. Fourre, M. Ishii, M. Bowker, Appl. Catal. B Environ. 45 (2003) 147–159.
[21] H. Abdulhamid, E. Fridell, M. Skoglundh, Top. Catal. 30–31 (2004) 161–168.
[22] T. Szailer, J.H. Kwak, D.H. Kim, J.C. Hanson, C.H.F. Peden, J. Szanyi, J. Catal. 239 (2006) 51–64.
[23] H. Abdulhamid, E. Fridell, M. Skoglundh, Appl. Catal. B Environ. 62 (2006) 319–328.
[24] I. Nova, L. Lietti, L. Castoldi, E. Tronconi, P. Forzatti, J. Catal. 239 (2006) 244–254.
[25] R. Burch, J.P. Breen, F.C. Meunier, Appl. Catal. B Environ. 39 (2002) 283–303.
[26] L. Olsson, R.J. Blint, E. Fridell, Ind. Eng. Chem. Res. 44 (2005) 3021–3032.
[27] L. Olsson, D. Monroe, R.J. Blint, Ind. Eng. Chem. Res. 45 (2006) 8883–8890.
[28] U. Tuttlies, V. Schmeisser, G. Eigenberger, Chem. Eng. Sci. 59 (2004) 4731–4738.
[29] C.M.L. Scholz, V.R. Gangwal, M. de Croon, J.C. Schouten, J. Catal. 245 (2007) 215–227.
[30] F. Laurent, C.J. Pope, H. Mahzoul, L. Delfosse, P. Gilot, Chem. Eng. Sci. 58 (2003) 1793–1803.
[31] A. Lindholm, N.W. Currier, E. Fridell, A. Yezerets, L. Olsson, Appl. Catal. B Environ. 75 (1–2) (2007) 78–87.
[32] A. Lindholm, N.W. Currier, A. Yezerets, L. Olsson, Top. Catal. 42–43 (2007) 83–89.
[33] J. Dawody, L. Eurenius, H. Abdulhamid, M. Skoglundh, E. Olsson, E. Fridell, Appl. Catal. A Gen. 296 (2005) 157–168.
[34] H.S. Fogler, Elements of Chemical Reaction Engineering, third ed., Prentice Hall, Englewood Clifs, 2001.
[35] B. Westerberg, E. Fridell, J. Mol. Catal. A Chem. 165 (2001) 249–263.
[36] E. Tronconi, P. Forzatti, AICHE J. 38 (1992) 201–210.
[37] R. Reid, The Properties of Gases and Liquids, fourth ed., McGraw–Hill, New York, 1987.
[38] J.A. Dumesic, D.F. Rudd, L.M. Aparicio, J.E. Rekoske, A.A. Trevino, The Microkinetics of Heterogeneous Catalysis, Am. Chem. Soc., Washington, DC, 1993.
[39] D.A. McQuarrie, Statistical Mechanics, Harper–Collins, New York, 1976.
[40] G. Herzberg, Electronic Spectra and Electronic Structure of Polyatomic Molecules, Van Nostrand Reinhold, New York, 1966.
[41] L. Lietti, P. Forzatti, I. Nova, E. Tronconi, J. Catal. 204 (2001) 175–191.
[42] J. Szanyi, J.H. Kwak, D.H. Kim, S.D. Burton, C.H.F. Peden, J. Phys. Chem. B 109 (2005) 27–29.
[43] F. Prinetto, G. Ghiotti, I. Nova, L. Lietti, E. Tronconi, P. Forzatti, J. Phys. Chem. B 105 (2001) 12732–12745.
[44] J. Dawody, S. Wall, E. Fridell, J. Mol. Catal. A Chem. 225 (2005) 259–269.
[45] V. Labalme, N. Guilhaume, E. Garbowski, M. Primet, Appl. Catal. A Gen. 133 (1995) 351–366.
[46] J. Dawody, M. Skoglundh, L. Olsson, E. Fridell, Appl. Catal. B Environ. 70 (2007) 179–188.
[47] L. Olsson, P. Jozsa, M. Nilsson, E. Jobson, Top. Catal. 42–43 (2007) 95–98.
[48] L. Olsson, M. Abul-Milh, H. Karlsson, E. Jobson, P. Thormahlen, A. Hinz, Top. Catal. 30–31 (2004) 85–90.
[49] L. Olsson, B. Westerberg, H. Persson, E. Fridell, M. Skoglundh, B. Andersson, J. Phys. Chem. B 103 (1999) 10433–10439.
[50] J.M. Coronado, J.A. Anderson, J. Mol. Catal. A Chem. 138 (1999) 83–96.
[51] P. Broqvist, I. Panas, H. Gronbeck, J. Phys. Chem. B 109 (2005) 15410–15416.
[52] H. Sjovall, L. Olsson, E. Fridell, R.J. Blint, Appl. Catal. B Environ. 64 (2006) 180–188.
[53] J.A. Miller, C.T. Bowman, Prog. Energy Combust. Sci. 15 (1989) 287–338.
[54] A.I.P. Elg, F. Eisert, A. Rosén, Surf. Sci. 382 (1997) 57.
[55] A.D. Kinnersley, G.R. Darling, S. Holloway, Surf. Sci. 377–379 (1997) 567–571.
[56] M.E. Bartram, R.G. Wirdham, B.E. Koel, Surf. Sci. 184 (1987) 57.
[57] G.B. Fisher, J.L. Gland, Surf. Sci. 94 (1980) 446–455.
[58] A. Johansson, M. Forsth, A. Rosen, Surf. Sci. 529 (2003) 247–266.
[59] S. Ljungstrom, B. Kasemo, A. Rosen, T. Wahnstrom, E. Fridell, Surf. Sci. 216 (1989) 63.
[60] J.M. Bradley, A. Hopkinson, D.A. King, Surf. Sci. 371 (1997) 255.
[61] L. Olsson, E. Fridell, J. Catal. 210 (2002) 340–353.
[62] L. Cumaranatunge, S.S. Mulla, A. Yezerets, N.W. Currier, W.N. Delgass, F.H. Ribeiro, J. Catal. 246 (2007) 29–34.